AGU PUBLICATIONS

Geochemistry, Geophysics, Geosystems

RESEARCH ARTICLE
10.1002/2015GC006246

Key Points:
- Use of InSAR for measuring interseismic deformation
- Estimation of InSAR uncertainties from comparison with independent GPS data
- Potentials and limits of InSAR for separating slip-rates on closely spaced faults

Supporting Information:
- Supporting Information S1

Correspondence to:
E. Chaussard,
estellec@buffalo.edu

Citation:
Chaussard, E., C. W. Johnson, H. Fattahi, and R. Bürgmann (2016), Potential and limits of InSAR to characterize interseismic deformation independently of GPS data: Application to the southern San Andreas Fault system, *Geochem. Geophys. Geosyst.*, *17*, 1214–1229, doi:10.1002/2015GC006246.

Received 31 DEC 2015
Accepted 23 FEB 2016
Accepted article online 1 MAR 2016
Published online 31 MAR 2016

Potential and limits of InSAR to characterize interseismic deformation independently of GPS data: Application to the southern San Andreas Fault system

E. Chaussard[1], C. W. Johnson[2,3], H. Fattahi[4], and R. Bürgmann[2,3]

[1]Department of Geology, State University of New York, Buffalo, New York, USA, [2]Department of Earth and Planetary Science, University of California, Berkeley, Berkeley, California, USA, [3]Berkeley Seismological Laboratory, University of California, Berkeley, California, USA, [4]Seismological Laboratory, California Institute of Technology, Pasadena, California, USA

Abstract The evaluation of long-wavelength deformation associated with interseismic strain accumulation traditionally relies on spatially sparse GPS measurements, or on high spatial-resolution InSAR velocity fields aligned to a GPS-based model. In this approach the InSAR contributes only short-wavelength deformation and the two data sets are dependent, thereby challenging the evaluation of the InSAR uncertainties and the justification of atmospheric corrections. Here we present an analysis using 7 years of Envisat InSAR data to characterize interseismic deformation along the southern San Andreas Fault (SAF) and the San Jacinto Fault (SJF) in southern California, where the SAF bifurcates onto the Mission Creek (MCF) and the Banning (BF) fault strands. We outline the processing steps for using InSAR alone to characterize both the short- and long-wavelength deformation, and evaluate the velocity field uncertainties with independent continuous GPS data. InSAR line-of-sight (LOS) and continuous GPS velocities agree within ~1–2 mm/yr in the study area, suggesting that multiyear InSAR time series can be used to characterize interseismic deformation with a higher spatial resolution than GPS. We investigate with dislocation models the ability of this mean LOS velocity field to constrain fault slip rates and show that a single viewing geometry can help distinguish between different slip-rate scenarios on the SAF and SJF (~35 km apart) but multiple viewing geometries are needed to differentiate slip on the MCF and BF (<12 km apart). Our results demonstrate that interseismic models of strain accumulation used for seismic hazards assessment would benefit from the consideration of InSAR mean velocity maps.

1. Introduction

Evaluating seismic hazard relies on accurate slip rate estimates considering both geologic and geodetic observations. Geologic data provide estimates for the past 10^4-10^6 years of fault activity, based on offsets of dated landforms to determine Holocene slip rates [*Burbank and Anderson*, 2001] and on paleoseismic trenching aimed at determining recurrence intervals and average slip for the most recent earthquakes [*McCalpin*, 2009]. Satellite geodesy measurements from GPS and InSAR provide a velocity field that is incorporated into a model to derive an interseismic slip rate estimate [e.g., *Segall*, 2002]. Interseismic slip rate models assume a steady state velocity field and transient effects from previous earthquakes are neglected or removed.

GPS measurements provide a temporally dense but spatially sparse data set for models to constrain interseismic fault slip parameters [e.g., *Murray et al*., 2014]. To address the limited spatial GPS coverage, InSAR velocity fields aligned to GPS-derived deformation models have been used [e.g., *Bürgmann et al*., 2006; *Fialko*, 2006; *Tong et al*., 2013; *Shirzaei and Bürgmann*, 2013] (see *Wright et al*. [2013, Table 4] for a compilation of these works). In this method the InSAR contribution is limited to constraining the short-wavelength deformation and the long-wavelength deformation signal is removed and replaced with a model derived from the GPS data. Thus, the characterization of interseismic deformation is limited to places with dense GPS networks and the data set dependency makes it impossible to use the GPS data to evaluate the uncertainty of InSAR data.

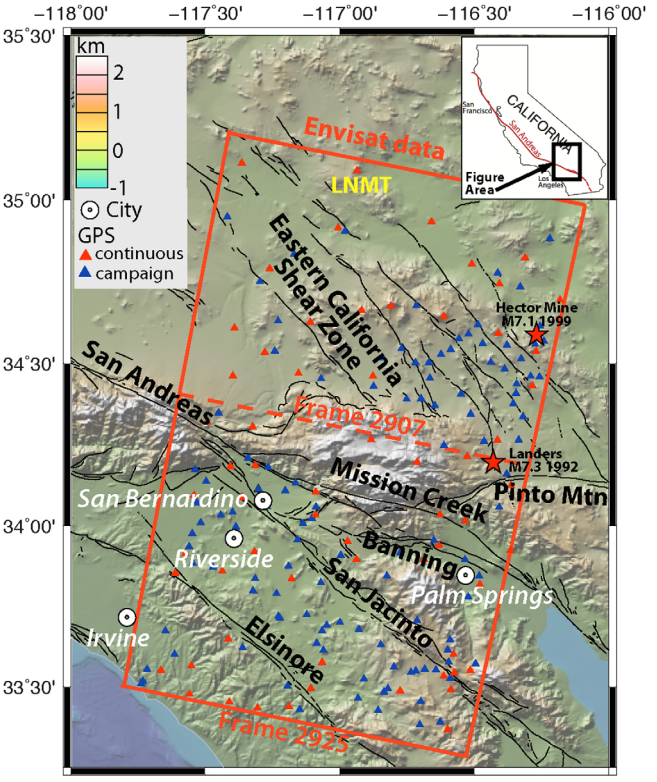

Figure 1. Topographic (background colors) and fault (black lines) map of the study area. The red rectangle is the footprint of the Envisat SAR data used for the analysis. Red and blue triangles show continuous GPS sites and campaign sites (CMM4), respectively with 63 continuous sites and 119 campaign sites. A pixel near the GPS station LNMT (yellow label) serves as reference point for the InSAR data. White dots indicate large cities. The two red stars indicate the epicenters of two large earthquakes (1999 Hector Mine and 1992 Landers) that occurred in the area.

Traditional InSAR processing techniques include the removal of a two-dimensional surface as either a phase ramp or a quadratic surface from each interferogram or each time-series epoch to reduce the effects of orbital errors. This procedure eliminates the long-wavelength interseismic strain signal from the InSAR data set. However, *Fattahi and Amelung* [2014] showed that the combination of tens to hundreds of SAR acquisitions does enable the detection of a long-wavelength deformation signal on the order of a few mm/yr per hundred kilometers when high-precision orbits are available. Thus, using time-series analysis techniques with many SAR acquisitions, the long-wavelength deformation should be resolvable with InSAR alone and no ramp should be removed during processing. Following this protocol, *Chaussard et al.* [2015b] showed that an InSAR-based interseismic velocity field provides better constraints for dislocation models of slip rates of the Hayward-Calaveras Faults in the San Francisco Bay Area compared to models relying only on GPS velocities. Additionally, *Chaussard et al.* [2015a] demonstrated that the uncertainty of the InSAR velocity field can be evaluated using the GPS data if the two remain independent.

Fault slip rates are estimated from geodetic data relying on three main types of models: block models, which consider a combination of rigid block rotations with kinematically consistent fault slip rates and locking depths [e.g., *Matsu'ura et al.*, 1986; *McCaffrey*, 2002; *Meade and Hager*, 2005], deep dislocation models, which assume semiinfinite screw dislocations buried in an elastic half-space [e.g., *Savage and Burford*, 1973; *Zeng and Shen*, 2014], and viscoelastic models, which incorporate viscoelastic rheologies into the interseismic deep dislocation model [e.g., *Savage and Prescott*, 1978; *Johnson et al.*, 2007]. The resolution of these models for slip rates on closely spaced faults is directly dependent on the spatial sampling of the data. Even in southern California, south of the Mojave Desert (Figure 1), where there is a dense GPS network, slip partitioning between the major faults of the San Andreas Fault (SAF) system remain a subject of debate.

Geodetic observations have shown that a total of 35–40 mm/yr of dextral motion is accommodated across the SAF, the San Jacinto Fault (SJF), and the Elsinore Fault (EF) in Southern California [*Johnson et al.*, 1994; *Bennett et al.*, 1996]. On one hand, geologic measurements suggest rates of 14–19 mm/yr on the SAF [*Van der Woerd et al.*, 2006; *Behr et al.*, 2010] and 11–20 mm/yr on the SJF [*Rockwell et al.*, 1990; *Blisniuk et al.*, 2010; *Kendrick et al.*, 2002; *Janecke et al.*, 2010]. On the other hand, geodetic estimates vary from equal rates of 14 mm/yr on the two faults [*Platt and Becker*, 2010], to significantly higher rates of 21–25 mm/yr on the SAF [*Meade and Hager*, 2005; *Fay and Humphreys*, 2005; *Becker et al.*, 2005; *Fialko*, 2006; *Spinler et al.*, 2010], to the SJF slipping up to 24 mm/yr and faster than the SAF [*Lundgren et al.*, 2009]. Additionally, at latitude 34°N the SAF bifurcates into the Mission Creek Fault (MCF) to the north and the Banning Fault (BF) to the south, separated by at most 12 km (Figure 1), and no agreement has been reached on which fault strand is currently the most active [*Behr et al.*, 2010; *Fumal et al.*, 2002; *Gold et al.*, 2015].

In this study we present short- and long-wavelength deformation resolved with Envisat InSAR data along the southern SAF. Throughout the processing the InSAR and GPS data remain independent in order to estimate the uncertainty of the InSAR measurements. This allows for the full potential of the high spatial resolution of InSAR to resolve interseismic deformation. The work presented herein addresses questions from the 2014 Southern California Earthquake Center Community Geodetic Model (CGM) Workshop [*Murray et al*., 2013], during which the community used the same data set to establish the limits of different InSAR processing schemes. We then investigate the ability of the obtained mean line of sight (LOS) velocity field to distinguish between different slip-rate scenarios on the SAF and SJF ($\sim$35 km apart) and on the MCF and BF ($<$12 km apart).

2. Data and Methods

2.1. Data and InSAR Processing

We use 41 SAR images acquired by the Envisat satellite of the European Space Agency between 2004 and 2011. The data are from frames 2907 and 2925 of descending track 399 (Figure 1) and were obtained through the WInSAR archive. Due to inconsistent frame acquisition start and stop lines, the frames are assembled as a single large frame and processed together to avoid a gap across the MCF and BF. We use the Modular SAR Processor software from Gamma Remote Sensing to generate Single Look Complex data and the ROI_PAC software [*Rosen et al*., 2004] to produce over 240 interferograms. The interferograms have a pixel size of 20 m (ground range) $\times$ 4 m (azimuth). We remove topographic contributions using the Shuttle Radar Topography Mission (SRTM) 1-arc second digital elevation model [*Farr et al*., 2007]. We coregister the interferograms of each frame to a master image and use the statistical-cost network-flow algorithm for phase unwrapping (SNAPHU) [*Chen and Zebker*, 2001]. We correct phase unwrapping errors using the phase closure technique [*Fattahi*, 2015; *Biggs et al*., 2007]. The sum of phase-unwrapped interferograms around a closed loop should be zero because the contributions from deformation, atmosphere and orbital errors cancel out. Thus, nonzero phase closure allows us to detect phase-unwrapping errors [*Biggs et al*., 2007]. Our use of this automatic detection is possible given the relatively small network of interferograms but remains computationally time consuming. We then reference all interferograms to the same pixel, collocated with the GPS station LNMT (Figure 1) to enable direct comparison between the mean InSAR velocity map and the GPS velocity field.

2.2. InSAR Time Series Analysis

The time-series are generated with a Small Baseline Subset (SBAS) selection approach to minimize the spatial and temporal baselines of a fully connected network of interferograms and estimate the phase velocity between each epoch and the subsequent one (Figure 2, left) [*Berardino et al*., 2002]. We use a spatial baseline threshold of 300 m and a temporal threshold of 1 year and consider the first acquisition as a temporal reference to obtain the phase time-series. We note that the selected SBAS network leads to a temporal coherence [*Pepe and Lanari*, 2006] of 0.5 in the area between the BF and MCF (black square on Figure 2, right). This temporal coherence is below the threshold of 0.7 usually selected for final pixel selection to eliminate pixels affected by phase-unwrapping errors [*Casu et al*., 2006*; Tizzani et al*., 2007*; Gourmelen et al*., 2010] (Figure 2, bottom row). To retain data in this area, we apply an alternative interferogram selection method that accounts for the level of spatial coherence in each interferogram (Figure 2, right) [*Chaussard et al*., 2015a, 2015b]. Only interferograms with a high percentage of pixels (50%) above a sufficient coherence (0.5) in our area of interest (black rectangle) are included in the time series analysis. This coherence-based selection leads to a temporal coherence of 0.8–0.9 for the region between the BF and MCF (Figure 2, right), which is necessary for having reliable deformation measurements between the two faults. A disadvantage of this method is that some interferograms and SAR acquisitions must be discarded due to low coherence (105 interferograms are kept, supporting information Table S1), as shown with the time series being referenced to 30 May 2005 (Figure 2, top row right), leading to a lower temporal sampling.

2.3. Postprocessing Corrections

We use the empirical model of *Marinkovic and Larsen* [2013] to correct the Local Oscillator drift (LOD) of the ASAR instrument and improve the geo-location accuracy of the sensor (Figure 3) [*Fattahi and Amelung*, 2014*; Chaussard et al*., 2015b]. The slow decay of the sensor's Local Oscillator frequency with respect to its nominal value leads to a linear and correlated-in-time phase trend corresponding to $\sim$15 mm/yr of

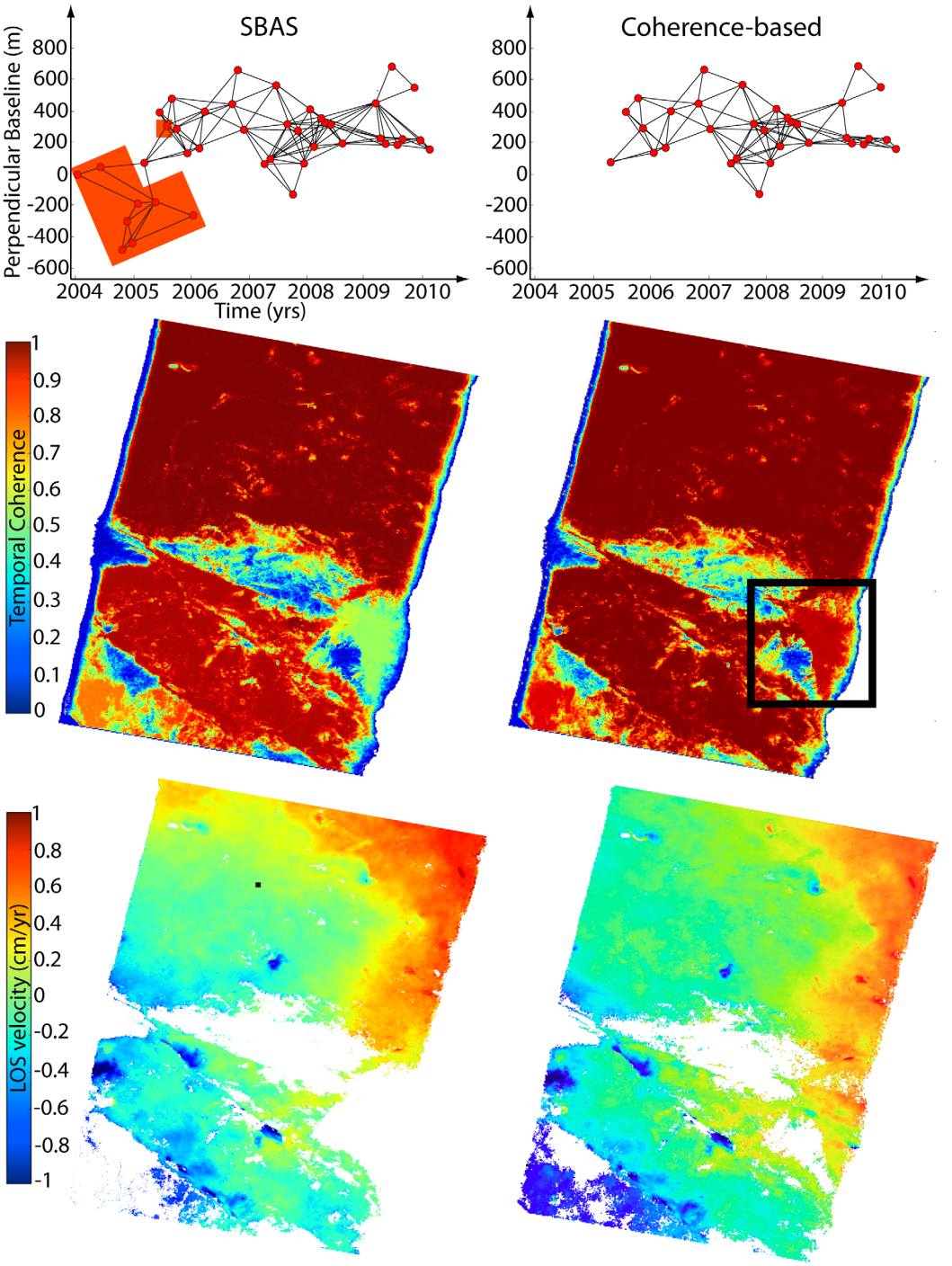

Figure 2. (left) Traditional SBAS time series analysis compared to (right) a coherence-based selection method. The top row shows the spatial baselines versus temporal baselines selected. The red boxes highlight the SAR acquisitions removed by the coherence-based selection. The middle row shows the resulting temporal coherence map. The bottom row shows the resulting mean velocity maps with a mask based on a temporal coherence threshold of 0.7. The area of interest between the MCF and the BF (black square) has a low temporal coherence (0.4–0.5) when performing a typical SBAS selection. A coherence-based selection for this area of interest leads to higher temporal coherence and is thus preferable for our purpose.

equivalent deformation (from near to far range) (Figure 3). The model used to correct the LOD adjusts the range change history for each pixel with a correction C of $C=(3.87 \times 10^{-7})x\delta\rho\delta t$ with x the dimensionless pixel count in range direction, $\delta\rho$ the range pixel size, and δt the time difference between a given epoch and the reference epoch. This linear correction is referenced to the same pixel as the InSAR data and

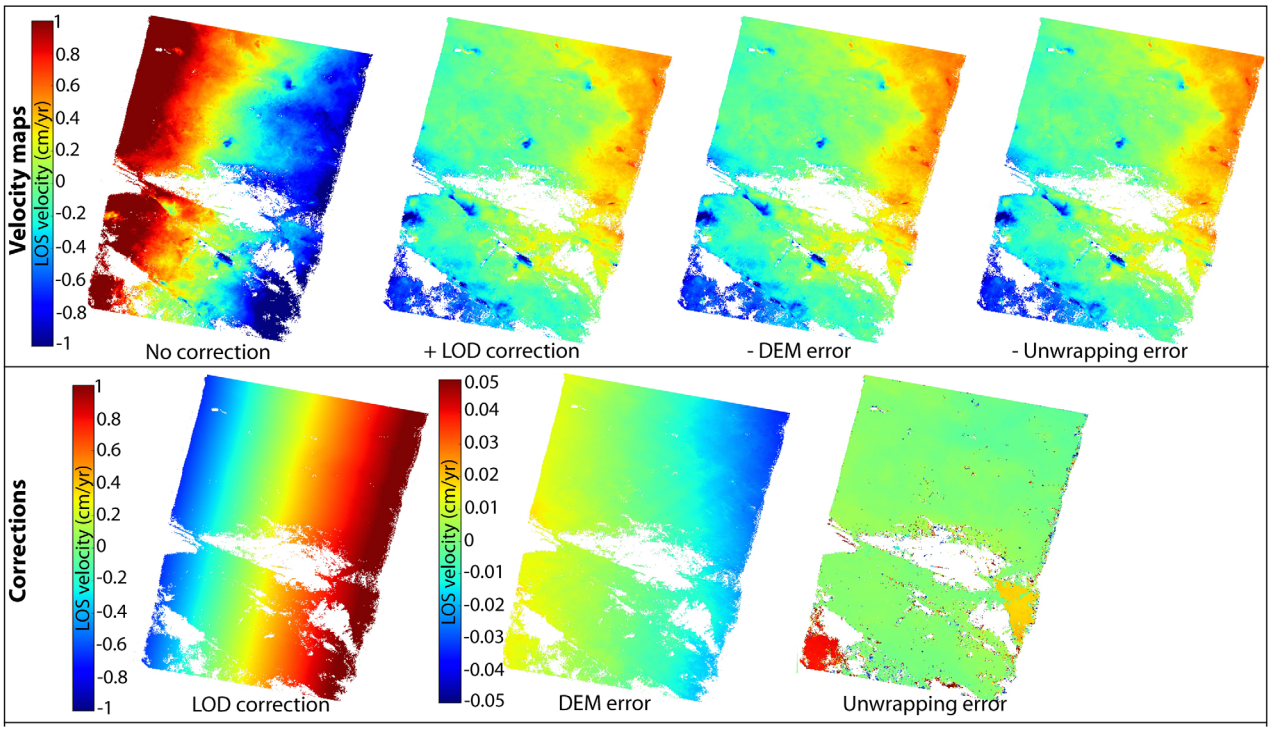

Figure 3. Necessary corrections to obtain a mean LOS velocity field that can be used to constrain interseismic deformation. The top row shows the mean velocity map after the different correction steps and the bottom row shows the corrections (difference between the velocity maps at the different steps).

removed from each epoch. Note that systematically removing a plane or quadratic function from each interferogram leads to different results than applying this empirical model (supporting information Figure S1).

The digital elevation model (DEM) introduces phase errors in the SBAS time series that are proportional to the perpendicular baseline history of the set of SAR acquisitions. To correct for topographic residuals we follow the method of *Fattahi and Amelung* [2013] and correct the time series dependency on the perpendicular baseline history in the time-domain. In our case, the DEM error correction estimates a gentle ramp (Figure 3). A likely explanation is that the calculated DEM error does not correspond to actual DEM errors, but to other geometrical phase residuals also proportional to the perpendicular baselines and introduced by imprecise imaging geometry in InSAR processing [*Fattahi and Amelung*, 2014] or timing errors [*Wang and Jonsson*, 2014]. The remaining phase histories in nondeforming areas contain contributions from remaining orbital errors and atmospheric delay.

Given the orbital accuracy of the Envisat satellite (uncertainties of 2 and 3–6 cm in vertical and horizontal direction, respectively [*Rudenko et al*., 2012; *Otten et al*., 2012]), the precision of the mean velocity map is on the order of 1 mm/yr/100 km, which enables detection of long-wavelength deformation if no ramp is removed during processing [*Fattahi and Amelung*, 2014]. Thus, the main source of remaining noise corresponds to atmospheric delay and further consideration of independent data should be used to estimate the need for additional corrections.

2.4. InSAR Atmospheric Noise

Given ground displacement as the signal of interest, the ionosphere and troposphere are the main sources of noise in InSAR displacement time-series measurements. The impact of ionosphere on the InSAR data are about 16 times greater for L-band (wavelength of ~24 cm) than C-band (wavelength of ~6 cm) SAR data [*Meyer and Nicoll*, 2008; *Rosen et al*., 1996] due to the frequency-dependency of the ionosphere refractive index. Thus, the ionospheric noise is a great impediment to studying interseismic deformation with L-band data (e.g., from JERS, ALOS-1, ALOS-2, and the future NiSAR mission) [e.g., *Liu et al*., 2014]. This large ionospheric contamination in L-band data is one of the reasons why recent studies using ALOS-1 data to study

interseismic deformation relied on GPS to constrain the longer-wavelength deformation [e.g., *Tong et al*., 2013]. Here we rely on C-Band Envisat data, which are minimally affected by ionospheric noise.

In C-Band, the uncertainty of the InSAR displacement time series is dominated by tropospheric delay [*Fattahi and Amelung*, 2015; *Jolivet et al*., 2011]. Tropospheric delays result from changes in the refractive index due to variations in atmospheric pressure, temperature and water vapor, with the water vapor being the largest concern [*Tarayre and Massonnet*, 1996; *Hanssen*, 2001]. Tropospheric delay can be separated into turbulent mixing due to water vapor distribution and vertical stratification of the atmosphere [*Zebker et al*., 1997; *Emardson et al*., 2003]. Tropospheric correction methods that assume a temporally random distribution of the delay use spatial-temporal filtering to reduce the tropospheric phase delay [*Ferretti et al*., 2001; *Hooper et al*., 2007]. Methods that assume that the deformation and tropospheric contributions are spatially uncorrelated rely on an empirical phase delay model based on the elevation of the terrain to correct the stratified tropospheric delay [e.g., *Remy et al*., 2003; *Biggs et al*., 2007; *Cavalié et al*., 2008; *Shirzaei and Burgmann*, 2012; *Lin et al*., 2010]. Other methods assimilate the estimated zenith wet delay from GPS observations [*Williams et al*., 1998; *Webley et al*., 2002; *Li et al*., 2006; *Onn and Zebker*, 2006] and meteorological observations in atmospheric models [*Wadge et al*., 2002; *Puysségur et al*., 2007] to predict the tropospheric delay in the InSAR data. The stratified delay has also been corrected using global atmospheric models such as ERA-Interim and MERRA that have spatial resolution of 10's of km. Lastly, precipitable water vapor products from the Moderate Resolution Imaging Spectroradiometer (MODIS) and the MEdium Resolution Imaging Spectrometer (MERIS) have been used to correct the tropospheric wet delay in InSAR data but they are limited to daytime SAR acquisitions in cloud-free conditions [*Li et al*., 2009, 2012; *Walters et al*., 2013]. Each method has limitations and therefore validation of the velocity field with independent data is recommended. In this study, we show that independent GPS data can be used to evaluate the uncertainty of InSAR velocities before tropospheric delay correction. One can use the same comparison to evaluate the uncertainty of InSAR data after each type of tropospheric delay correction, which is beyond the goals of this paper.

3. InSAR Potential for Characterization of Interseismic Deformation and Evaluation of Uncertainties

3.1. Comparison Between InSAR and Continuous GPS Data

We compare the InSAR mean velocities with independent GPS observations to validate that the mean InSAR velocity map can be used to constrain interseismic deformation and to evaluate its uncertainty due to the tropospheric delay. We use the time series from continuously operating GPS stations (cGPS) in the IGS08 reference frame (GPS-based realization of global secular frame ITRF2008 [*Blewitt et al*., 2013]) later referenced to LNMT to compare with the InSAR mean velocity field. We use daily processed solutions produced by the University of Nevada, Reno (UNR; http://geodesy.unr.edu/index.php). We estimate the cGPS velocities from the period overlapping the InSAR time series and project them into the corresponding InSAR line of sight (LOS) measurements. First, we use only the horizontal cGPS velocities to project to LOS (2-D GPS), considering that the horizontal cGPS components have lower uncertainties than the vertical (Figure 4, left). We also consider the horizontal and vertical cGPS components (3-D GPS) to project to LOS velocities (Figure 4, right). We compare the cGPS-derived LOS velocities with measured InSAR velocities using the mean of all pixels within 200 m from each cGPS station (Figure 4). The cGPS data uncertainties are shown with a 95% confidence level. Only a limited number of methods exist to evaluate the uncertainties of an InSAR mean velocity field. Some methods use the "undeforming" part of a velocity field to calculate the covariance structure of interferograms [e.g., *Lohman and Simons*, 2005]. However, we do not wish to assume part of the velocity field as "undeforming" and instead consider the InSAR uncertainties as being 2 mm/yr over 100 km (error bars in Figure 4), based on the orbital errors and tropospheric delay [*Fattahi and Amelung*, 2014, 2015]. We then use the comparison between the InSAR and cGPS data to evaluate the accuracy of the InSAR measurements.

We confirm that a good agreement exists between the InSAR and cGPS velocities with a correlation larger than 0.8 and an average absolute deviation (AAD) of 1.1 and 1.6 mm/yr for 3-D GPS LOS and 2-D GPS LOS, respectively. The overall agreement between the InSAR and cGPS data confirms that InSAR accurately characterizes the long-wavelength interseismic deformation. The agreement improves when the vertical

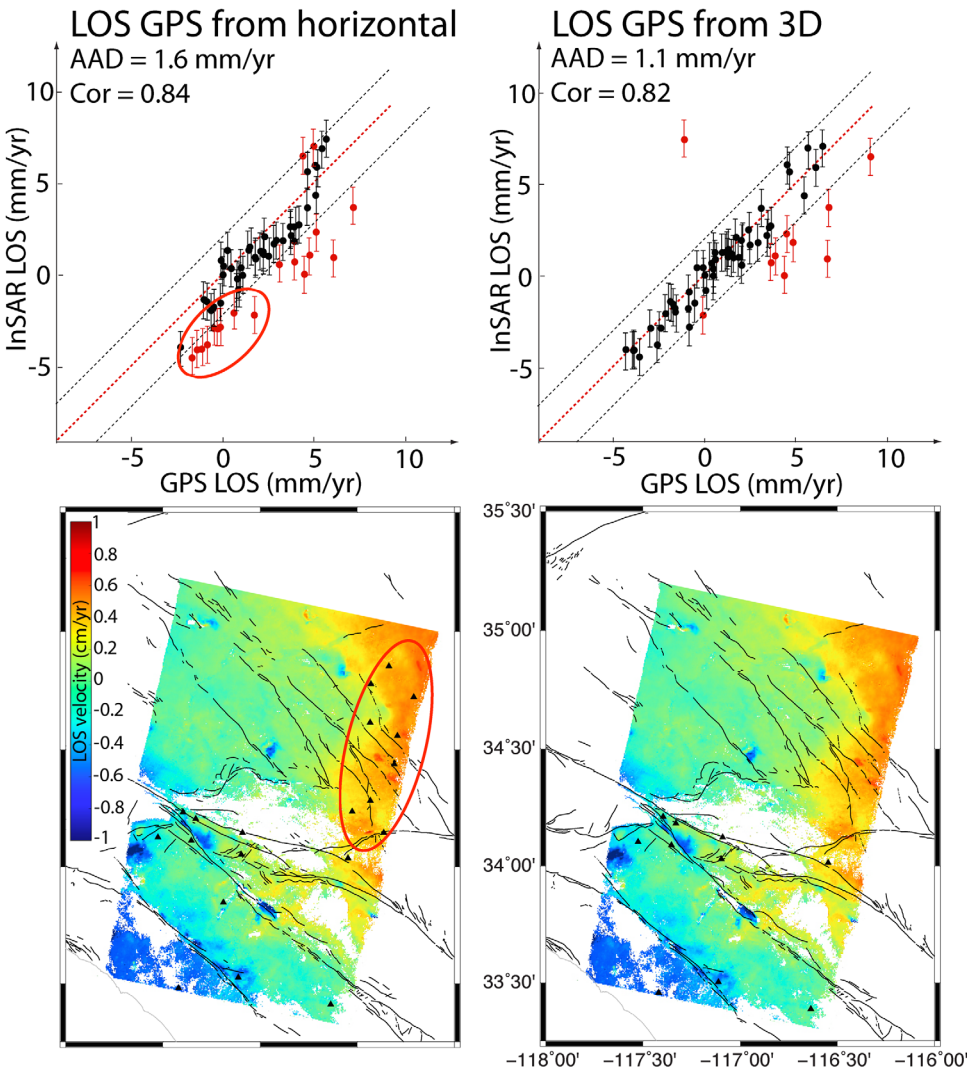

Figure 4. Comparison between InSAR LOS data at the locations of the cGPS sites and cGPS data projected to LOS from (left) horizontal only and (right) horizontal and vertical components. The red dashed line represents perfect agreement and the grey dashed lines show deviation of 2 mm/yr. The sites in red differ by more than 2 mm/yr and their locations are shown on the mean velocity maps below (same InSAR mean velocity field on the right and left). cGPS sites located within the red area in the InSAR mean velocity map (motion toward the satellite) are in better agreement with the InSAR data when considering the vertical component of the cGPS data (right).

component of the cGPS is included for transformation into LOS (Figure 4). The sites for which the InSAR-cGPS agreement improves are located in the red area of the mean velocity map (Figure 4, bottom row, circled area), confirming that this signal is real and corresponds to uplift also detected by cGPS. The sites for which the InSAR LOS velocities differ by more than 2 mm/yr from the cGPS LOS velocities (red in Figure 4 top row, locations shown in Figure 4 bottom row) are located at the border of the masked areas of the mean velocity map. This suggests that the InSAR pixels in these locations may be affected by remaining unwrapping errors.

3.2. Influence of the GPS Data Processing

We compare cGPS velocities derived from 2005 to 2011 time series made available by UNR with data processed by New Mexico Tech (NMT), Central Washington University (CWU), and the combined NMT-CWU solution of the Plate Boundary Observatory (PBO) to our InSAR results (Figure 5). We notice a significant difference between the different velocity products, especially in the vertical component. These discrepancies result from different processing algorithms as well as the applied corrections for tropospheric models, seasonal filtering, and postseismic corrections. The velocities calculated from the time series for the period

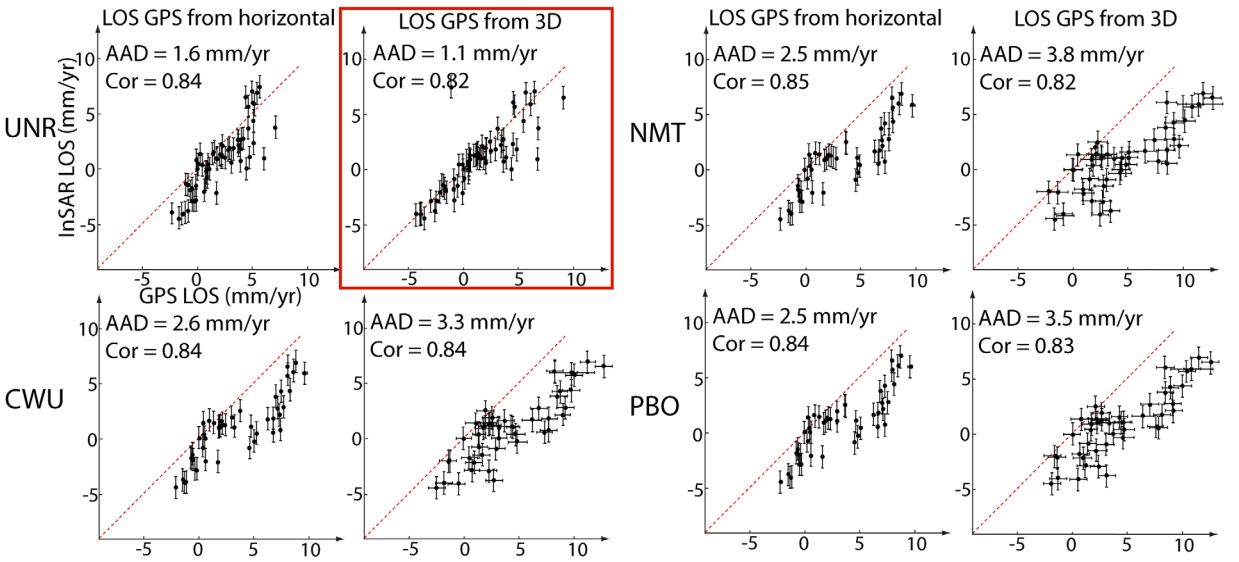

Figure 5. Comparison between the InSAR-cGPS agreement for cGPS velocities calculated from 2005 to 2011 time series from four different centers UNR, NMT, CWU, and PBO.

of the InSAR data provide a better agreement between the two data sets (Figure 5) than using the velocity products produced by the processing centers (supporting information Figure S2). This reflects that the GPS time series do not have as many corrections as the long-term velocities (e.g., PBO time series are not corrected for postseismic deformation but the PBO GPS velocities are). In this area of southern California two large earthquakes occurred in the past 30 years, the M7.3 Landers earthquake in 1992 and the M7.1 Hector Mine earthquake of 1999 (Figure 1). The postseismic corrections likely influence the agreement with the InSAR data. It is possible that the observed uplift area in the east of the velocity map (red on Figure 4) corresponds to a postseismic viscoelastic relaxation signal [*Freed et al*., 2007; *Pollitz*, 2015] that was accounted for and removed in various ways from some of the processed GPS velocity data (CWU, NMT, PBO) but is not removed from the InSAR velocity field. The higher temporal sampling of 3-D deformation by the cGPS time series allows for recognition of postseismic transients, while the InSAR mean velocity maps enable characterization of the spatial extent of the affected areas. For the purpose of estimating long-term interseismic fault slip rates, the knowledge of this transient signal is relevant and points to the synergy of the two methods.

3.3. InSAR Spatial Sampling Compared to Campaign GPS Data

Our results indicate that the InSAR derived LOS velocity field agrees with cGPS-derived rates within 1–2 mm/yr across the southern SAF without a priori information of the long-wavelength deformation (Figure 4). We now compare the InSAR mean velocities and spatial resolution to campaign GPS data, which have larger uncertainties and only horizontal measurements. Figure 1 shows the spatial sampling of the GPS with an average station spacing of ∼10–15 km while the InSAR mean velocity map provides hundreds of thousands of pixels where deformation can be measured. Figure 6 shows seven profiles on the eastern side of the mean velocity map spanning the MCF, BF, and SJF. We confirm a good agreement between the GPS (triangles) and InSAR data (black dots), using both cGPS (red triangles) and the Crustal Motion Model (CMM4) velocity field [*Shen et al*., 2011] from campaign GPS (blue triangles). The increased spatial sampling of the InSAR mean velocity map is most informative between neighboring fault strands (BF, MCF, Figure 6) where no GPS data are available. Only a few gaps exist in the mean InSAR velocity map due to loss of coherence in high topography areas. Our results thus clearly demonstrate that InSAR provide better spatial constraints for interseismic deformation than GPS.

3.4. InSAR Uncertainties Relative to the Topography

We now test whether the InSAR-cGPS discrepancies are correlated with the topography, which would suggest the presence of a stratified tropospheric delay in the InSAR mean velocity map requiring further correction. Figure 7 shows the cGPS-InSAR LOS-rate difference versus the cGPS stations elevation considering 2-D

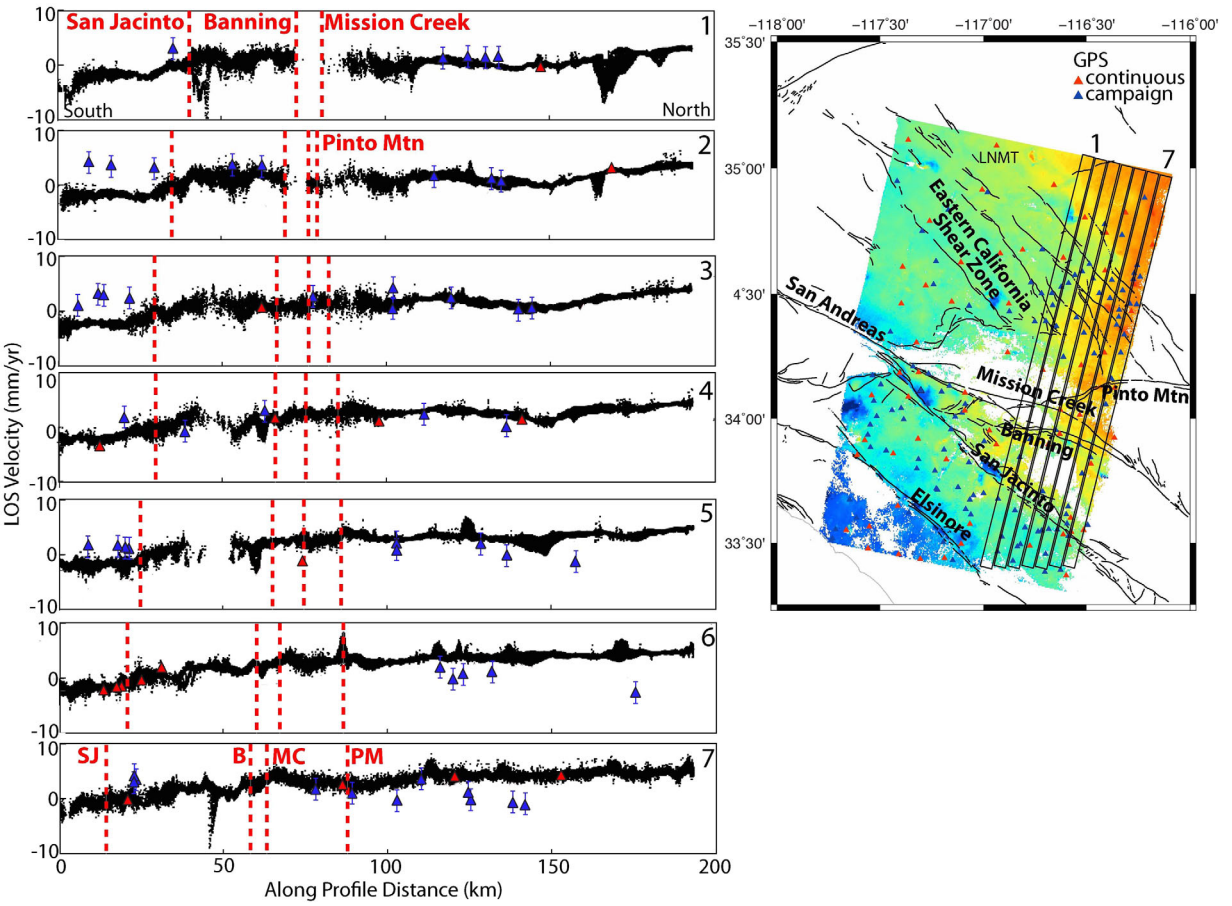

Figure 6. Transects comparing InSAR (black) and GPS (red triangles, continuous and blue triangles, campaign sites (e.g., CMM4)) velocities in the SAF, SJF, BF, and MCF area. The red dash lines show the locations of the faults on the transect and highlight that despite the high spatial resolution of the InSAR data, separating strain accumulation on neighboring fault strand is challenging. The map on the right shows the locations of the profiles 1–7 (rectangles), of the GPS sites and of the faults.

(left) and 3-D (right) UNR cGPS data. There is no clear trend, suggesting that the stratified tropospheric delay is not responsible for the InSAR-cGPS discrepancies. Thus, in this case the mean velocity map is not affected by a significantly stratified tropospheric delay. This is likely due to the large number of interferograms, the relatively modest topography of the area, and the fact that the InSAR data are decorrelated at the highest elevations where cGPS stations are sparse (north of the MCF, Figure 1). Our results thus

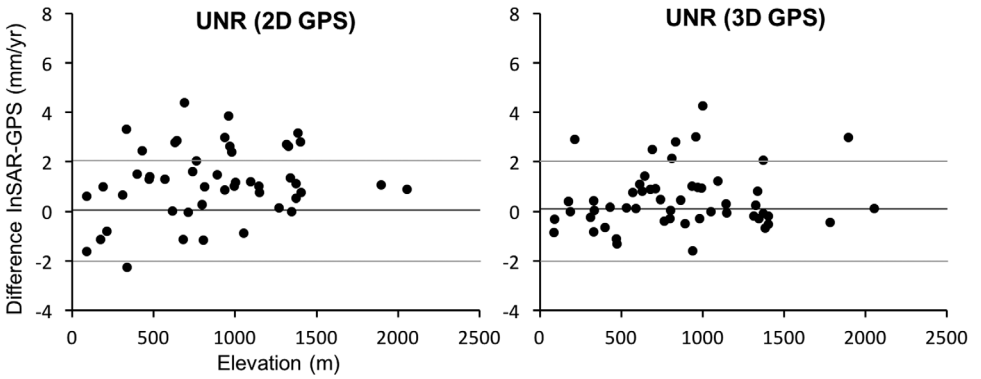

Figure 7. GPS-InSAR LOS-rate difference versus the GPS stations elevation considering 2-D (left) and 3-D (right) cGPS data from UNR. The lack of trend suggests that the stratified tropospheric delay is not responsible for the InSAR-cGPS discrepancies.

demonstrate that the comparison between InSAR and independent GPS data enables characterization of the noise level and noise source of the mean velocity map.

3.5. InSAR Uncertainties From MODIS Observations

Using MODIS data we independently estimate the scattering of each pixel's time series due to the stochastic wet delay [*Fattahi and Amelung*, 2015]. We obtain MODIS time-series of delay for all acquisitions from 2002 to 2012 (two acquisitions per day, total ~7000 acquisitions), remove the seasonal effects and calculate the standard deviation [*Fattahi and Amelung*, 2015]. The uncertainty of the velocity field is then obtained by considering the SAR acquisition times (Figure 8b). The results indicate the average standard deviation of the stochastic wet delay is ~2 mm/yr, in agreement with the absolute average deviation between the cGPS and InSAR data. The maximum standard deviation of the stochastic wet delay is ~4 mm/yr observed between the MCF and BF. The plot of the velocity uncertainties versus distance allows us to constrain the uncertainty between any two pixels when knowing their distance (Figure 8c). It was generated using a sample of 1000 pixels in the region, each pixel being considered as reference once, calculating the uncertainties and distances of all other pixels, and then moving the reference pixel to the next pixel and repeating the calculations. The plot shows that uncertainties are increasing with distance and flatten at distances of

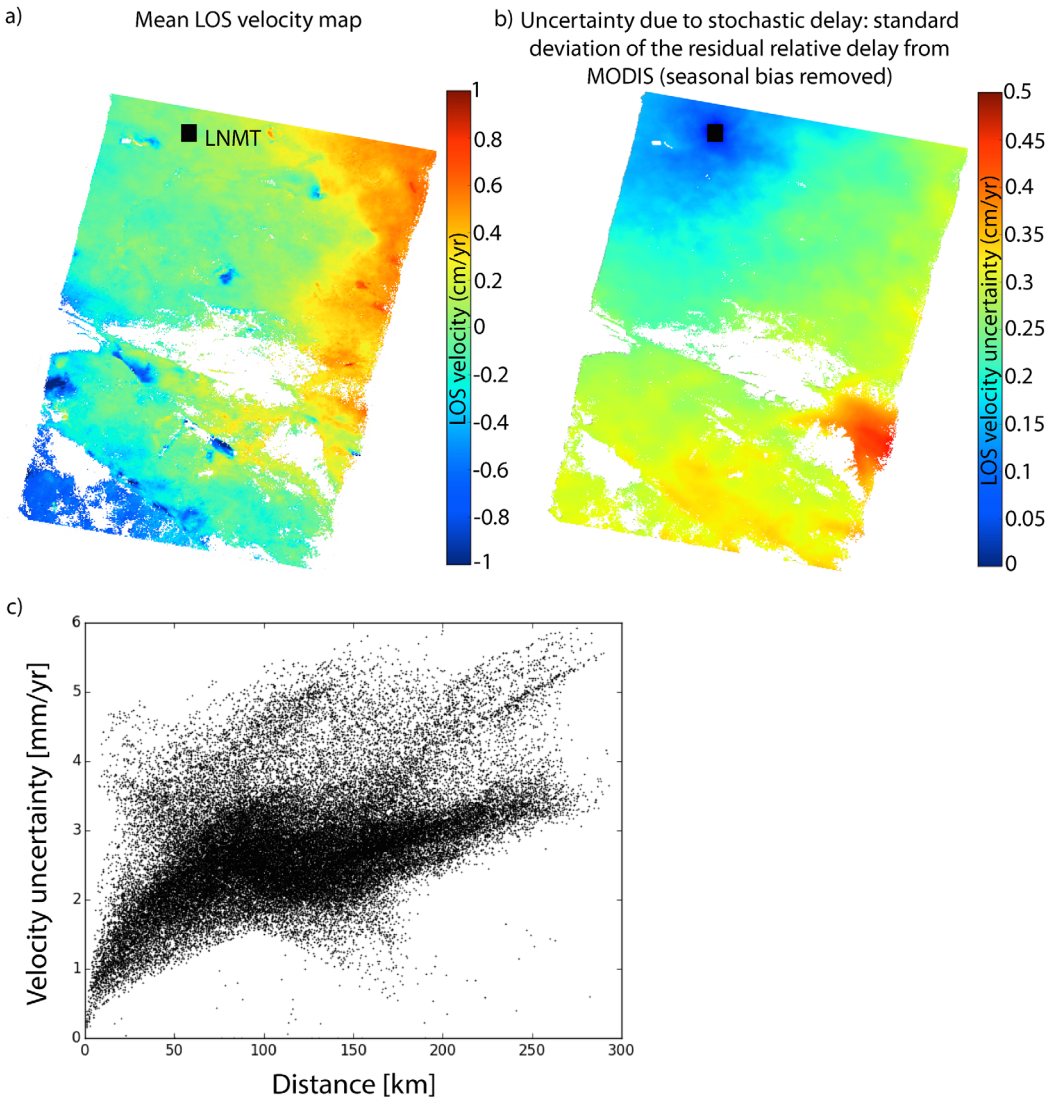

Figure 8. Comparison between the mean LOS velocity map (a) and the uncertainties due to the stochastic tropospheric wet delay (b). The uncertainties correspond to the standard deviation of the residual relative delay from MODIS after removing the seasonal bias. c) Velocity uncertainties as a function of the distance between two pixels (sample of 1000 pixels in the area).

~80 km with an average ~2.5 mm/yr. Thus, we confirm with independent MODIS data that the average noise level due to tropospheric delay is low in our study area and that InSAR enables imaging of short and long wavelength deformation on the order of 2 mm/yr.

4. InSAR Limitations to Characterize Interseismic Deformation

We showed that InSAR is able to characterize the interseismic deformation that is traditionally measured with spatially sparse GPS data. However, three limitations of using InSAR to characterize interseismic deformation exist. The first is that measurements are in LOS direction rather than providing horizontal or 3-D components. To decompose the InSAR LOS signal into its vertical and horizontal components requires sufficient acquisitions of both ascending and descending SAR data [*Wright et al*., 2004]. However, in this location the Envisat ascending data are sparse. The second limitation is that the amplitude of the measured interseismic deformation in LOS depends on the SAR acquisition geometry with respect to the fault orientation. InSAR measurements are insensitive to horizontal displacements in the along-track direction. In this study the most favorably oriented fault is the MCF (~N75°W or 85° from the SAR azimuth direction of ~N166°W), and the orientation becomes less favorable for the SAF and BF (~N65°W or ~75° from the SAR azimuth direction) and the SJF (~N50°W or ~60° from the SAR azimuth direction). This indicates that a fraction of the interseismic deformation associated with these faults will not be captured by the descending LOS data. The third limitation for resolving interseismic deformation is the large number of SAR acquisitions required to generate a dense time series both temporally (to decrease the effect of orbital errors) and spatially. The distance of these measurements need to extend at least five times the locking depth from the fault [*Savage and Burford*, 1973] to capture 90% of the interseismic deformation. For large fault systems this requires multiple SAR frames to be processed. The generation of a continuous velocity field can be problematic when frame borders are inconsistent with each other or with the neighboring frames.

5. Interseismic Deformation From InSAR on the Southern San Andreas Fault System

We test if the high spatial resolution of the InSAR data can help refine the slip estimates on the SAF and SJF separated by ~35 km with only descending-orbit LOS observations. We use forward dislocation models to produce mean LOS velocity fields considering different slip scenarios and test if the difference is resolvable with InSAR. The purpose of this paper is not to develop detailed modeling and reach precise estimates of fault slip rates, fault parameters or their uncertainties. Instead we illustrate with simple tests the cases for which the consideration of InSAR interseismic data can help differentiate between different slip models. We invert for slip rates on 3000 km deep vertical faults to approximate screw dislocations to infinite depth [*Savage and Burford*, 1973]. The faults are considered vertical and extend far away from the area of interest to avoid side effects. The faults and their slip rates are based on mean estimates from the Uniform California Earthquake Rupture Forecast or UCERF3 [*Field et al*., 2014]. We include the Elsinore Fault with a slip rate of 5 mm/yr and the Homestead Valley Fault and Lavic Lake Fault in the Eastern California Shear Zone (ECSZ), the two faults with the Landers and Hector Mine earthquake hypocenters, respectively, with slip rates of 3.5 and 3.4 mm/yr. We then use five different slip scenarios for the SAF and SJF (see supporting information Figure S3). The first two consider similar rates on the SAF and SJF either at 14 mm/yr (model 1) [*Platt and Becker*, 2010] or at 18 mm/yr on SAF and 19 mm/yr on SJF (model 2) [*Lindsey and Fialko*, 2013]. The third and fourth scenarios consider significantly higher slip rates on the SAF than on the SJF with 25 mm/yr on the SAF and 21 mm/yr on the SJF (model 3) [*Fialko*, 2006] and 25 mm/yr on the SAF and 12 mm/yr on the SJF (model 4) [*Fay and Humphreys*, 2005]. The last scenario considers higher slip rates on the SJF than the SAF with 24 mm/yr and 16 mm/yr, respectively (model 5) [*Lundgren et al*., 2009] (see supporting information Figure S3 for synthetic mean LOS velocity maps).

We use profiles crossing the faults to compare the different modeled velocities and the InSAR data (Figure 9). We observe that the difference in mean velocity produced by the different models is large enough (3 to 7 mm/yr, Figure 9 and supporting information Figure S3) that InSAR could help favor a particular slip scenario. In all three profiles the 14 mm/yr of slip on the SAF and the SJF model is the closest to the observed mean velocity and, presumably, the difference between the model and the InSAR data relates to unmodeled postseismic effects. The vertical deformation in the mean LOS velocity map located north of the SAF (red on the

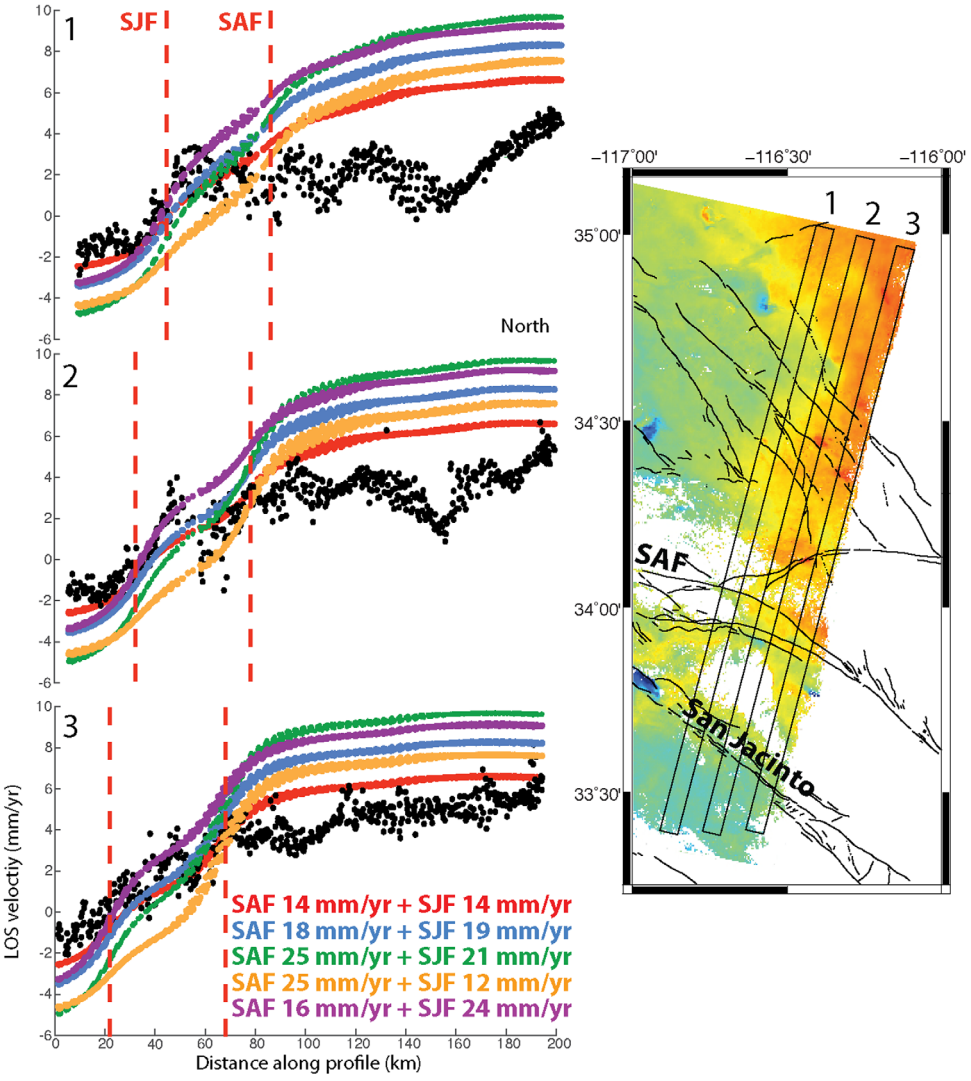

Figure 9. Profiles showing how the observed InSAR LOS velocity gradient and scatter compares with the five forward models described in the text and with the mean velocity fields shown in supporting information Figure S3 (see legend for corresponding colors).

right side, Figure 9), is likely to be associated with late-stage postseismic viscoelastic relaxation [*Freed et al.*, 2007; *Pollitz*, 2015], which would need to be accounted for to accurately estimate the long-term slip rates.

In the first (westernmost) profile there is no clear localized velocity gradient associated with either the BF or MCF strand of the SAF system, but the gradient across the BF and MCF increases in the second and third profiles moving eastward. This suggests that slip rates may vary laterally, in agreement with block models suggesting lower slip rates in the Mojave section of the SAF than north and south of it [*Meade and Hager*, 2005; *Becker et al.*, 2005; *Spinler et al.*, 2010]. Overall, our simple forward models confirm that the high spatial resolution of the InSAR mean velocity map should help improve slip rate constraints on the SAF and SJF located 35 km apart since the predicted surface deformation from the different slip models is larger than the uncertainties in the InSAR mean velocity map.

In the previous forward models we considered the SAF with a single strand following the MCF. However, in the eastern part of our study area the SAF is separated into the BF and the MCF. The slip rates of these faults remain highly debated with works considering that the BF is the active strand of the SAF, the MCF being abandoned [*Fumal et al.*, 2002], while others consider the opposite [*Behr et al.*, 2010; *Blisniuk et al.*, 2013]. GPS data cannot help provide slip-rate estimates for these faults due to their close proximity (maximum of 12 km apart) and the lack of spatial sampling [*Liu et al.*, 2015] (Figure 6). We use forward dislocation models

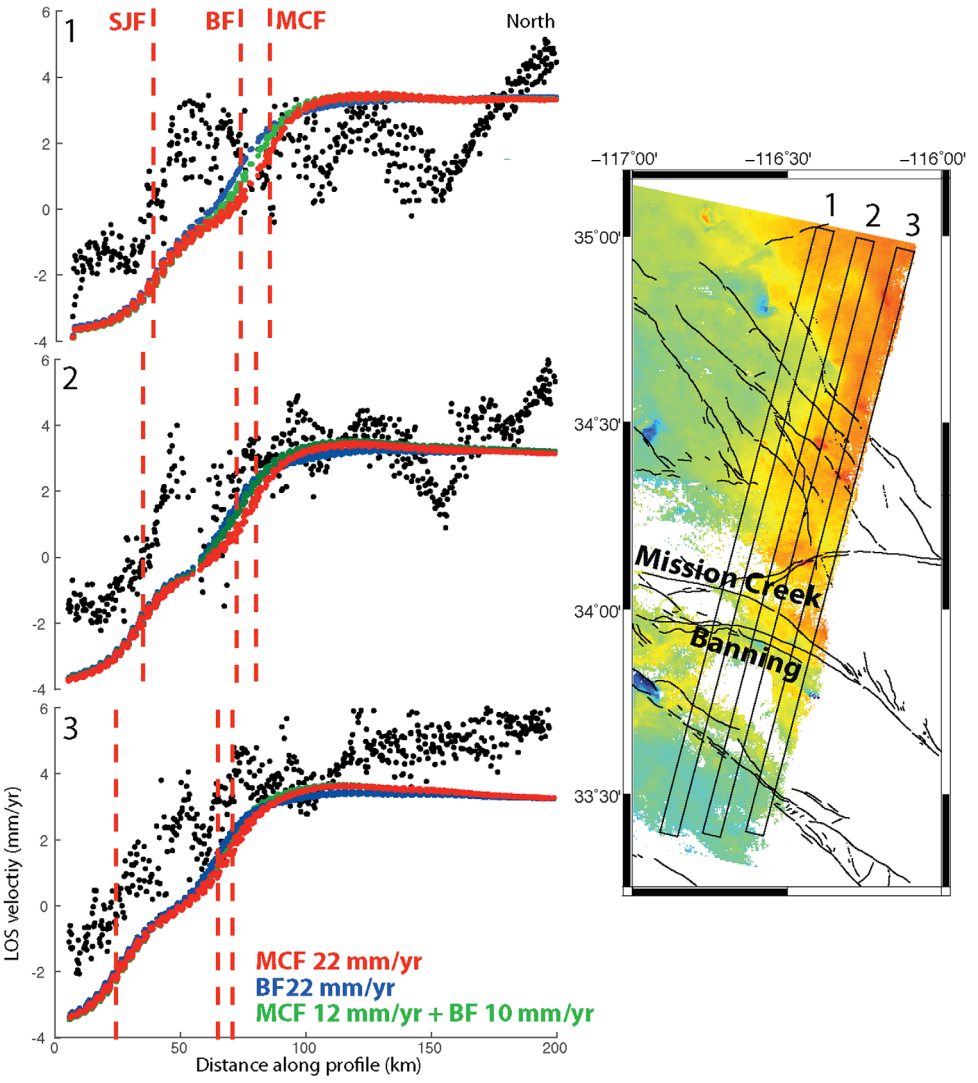

Figure 10. Profiles showing how the observed InSAR LOS velocity gradient and scatter compares with the three forward models described in the text and with the mean velocity fields shown in supporting information Figure S4 (see legend for colors).

to obtain mean LOS velocity maps considering three different slip scenarios on these two faults (supporting information Figure S4). The three slip scenarios consider 1) similar slip on the MCF (12 mm/yr) and the BF (10 mm/yr); 2) all the slip being accommodated on the BF (22 mm/yr); and 3) all the slip being accommodated on the MCF (22 mm/yr) (from UCERF3). Figure 10 and supporting information Figure S4 show that theses different slip scenarios for the BF and MCF are not resolvable with the LOS mean velocity map. The variation between the different models (red, green, and blue lines on Figure 10) is significantly smaller (<1 mm/yr) than the scattering and uncertainties of the InSAR data. Thus, in the case of closely spaced faults (<20 km) such as the BF and MCF, even the high spatial resolution of InSAR cannot help differentiate between different slip rate scenarios. We also test if this could be overcome by using a fault-parallel mean velocity map (supporting information Figure S5). In this case the different slip scenarios result in differences of mean fault-parallel velocity of up to 3 mm/yr. These results suggest that if multiple satellite viewing geometries were available to decompose the InSAR LOS signal into its vertical and horizontal components it may be possible to favor one slip scenario and provide geodetic constraints for the slip rates on the BF and MCF from InSAR data. Unfortunately, in this particular area the Envisat ascending data are sparse. Our results however demonstrate that advanced modeling efforts oriented toward characterization of fault slip rates will benefit from the incorporation of InSAR data, after examination of its level of uncertainties, as envisioned in the SCEC Community Geodetic Model (CGM) [*Murray et al.*, 2013].

6. Conclusion

We demonstrate that InSAR time series products can be used to measure long-wavelength deformation without the use of a priori GPS information during InSAR processing. We show that our InSAR LOS-velocity field agrees well with a long-wavelength GPS velocity field, and, by keeping InSAR and GPS data independent, we can evaluate the uncertainty of the InSAR mean velocity map. In the case of southern California, the InSAR and GPS-derived LOS velocities agree within 1–2 mm/yr consistent with the predicted InSAR uncertainties due to the wet delay based on independent MODIS observations We show that the high spatial resolution of InSAR provides additional data to improve estimates of long-term fault slip rates. Our first-order modeling shows that descending LOS Envisat data can help differentiate between various scenarios of slip partitioning on the SAF and SJF, separated by a maximum of $\sim$35 km, and can augment future modeling efforts. Our results also reveal that in the case of closely spaced faults ($<$12 km), such as the MCF and BF strands of the SAF, a single viewing geometry is not sufficient to separate the contributions from the two faults, but additional viewing geometries might provide enough constraints. Accordingly, it is important that current and future satellite missions consider acquiring data in multiple viewing geometries so that the InSAR LOS signal can be decomposed into its vertical and horizontal components and InSAR becomes fully integrated into interseismic models of strain accumulation used for seismic hazards assessment.

Acknowledgments

We thank the National Aeronautics and Space Administration (NASA) for support through grant NNX12AQ32G and the U.S. Geological Survey National Earthquake Hazards Reduction Program (NEHRP) for support through grants G12AP20096 and G13AP00035. C. W. Johnson is supported by the NSF Graduate Research Fellowship Program through grant DGE1106400. The Envisat original data are copyrighted by the European Space Agency and were provided through the WInSAR archive. We thank three anonymous reviewers and Thorsten Becker for review comments that helped improve the paper. We thank the State University of New York at Buffalo Center for Computational Research for access to their computing resources for processing.

References

Becker, T. W., J. L. Hardebeck, and G. Anderson (2005), Constraints on fault slip rates of the southern California plate boundary from GPS velocity and stress inversions, *Geophys. J. Int.*, *160*(2), 634–650, doi:10.1111/j.1365-246X.2004.02528.x.

Behr, W. M., et al. (2010), Uncertainties in slip-rate estimates for the Mission Creek strand of the southern San Andreas fault at Biskra Palms Oasis, southern California, *Geol. Soc. Am. Bull.*, *122*(9–10), 1360–1377, doi:10.1130/B30020.1.

Bennett, R. A., W. Rodi, and R. E. Reilinger (1996), Global positioning system constraints on fault slip rates in southern California and northern Baja, Mexico, *J. Geophys. Res.*, *101*, 21,943–21,960.

Berardino, P., G. Fornaro, R. Lanari, and E. Sansosti (2002), A new algorithm for surface deformation monitoring based on small baseline differential SAR interferograms, *IEEE Trans. Geosci. Remote Sens.*, *40*(11), 2375–2383, doi:10.1109/TGRS.2002.803792.

Biggs, J., T. J. Wright, Z. Lu, and B. E. Parsons (2007), Multi-interferogram method for measuring interseismic deformation: Denali fault, Alaska, *Geophys. J. Int.*, *170*(3), 1165–1179.

Blewitt, G., C. Kreemer, W. C. Hammond, and J. M. Goldfarb (2013), Terrestrial reference frame NA12 for crustal deformation studies in North America, *J. Geodynamics*, *72*, 11–24, doi:10.1016/j.jog.2013.08.004.

Blisniuk, K., T. Rockwell, L. A. Owen, M. Oskin, C. Lippincott, M. W. Caffee, and J. Dortch (2010), Late Quaternary slip rate gradient defined using high-resolution topography and 10Be dating of offset landforms on the southern San Jacinto Fault zone, California, *J. Geophys. Res.*, *115*, B08401, doi:10.1029/2009JB006346.

Blisniuk, K., K. Scharer, W. Sharp, R. Bürgmann, M. Rymer, and P.Williams (2013), New geologic slip rate estimate for the Mission Creek fault zone, Southern California Earthquake Center Annual Meeting Proceedings and Abstracts, SCEC, vol. 23, 97 pp.

Burbank, D. W., and R. S. Anderson (2001), *Tectonic Geomorphology*, Blackwell, Malden, Mass.

Bürgmann, R., G. Hilley, A. Ferretti, and F. Novali (2006), Resolving vertical tectonics in the San Francisco Bay Area from permanent scatterer InSAR and GPS analysis, *Geology*, *34*(3), 221, doi:10.1130/G22064.1.

Casu, F., M. Manzo, and R. Lanari (2006), A quantitative assessment of the SBAS algorithm performance for surface deformation retrieval from DInSAR data, *Remote Sens. Environ.*, *102*(3–4), 195–210, doi:10.1016/j.rse.2006.01.023.

Cavalié, O., C. Lasserre, M. P. Doin, G. Peltzer, J. Sun, X. Xu, and Z. K. Shen (2008), Measurement of interseismic strain across the Haiyuan fault (Gansu, China), by InSAR, *Earth Planet. Sci. Lett.*, *275*(3), 246–257.

Chaussard, E., R. Bürgmann, H. Fattahi, R. M. Nadeau, T. Taira, C. W. Johnson, and I. Johanson (2015a), Potential for larger earthquakes in the East San Francisco Bay Area due to the direct connection between the Hayward and Calaveras Faults, *Geophys. Res. Lett.*, *42*, 2734–2741, doi:10.1002/2015GL063575.

Chaussard, E., R. Bürgmann, H. Fattahi, C. W. Johnson, R. Nadeau, T. Taira, and I. Johanson (2015b), Interseismic deformation and refined earthquake potential on the Hayward-Calaveras fault zone, *J. Geophys. Res. Solid Earth*, *120*, 8570–8590, doi:10.1002/2015JB012230.

Chen, C. W., and H. A. Zebker (2001), Two-dimensional phase unwrapping with use of statistical models for cost functions in nonlinear optimization, *J. Opt. Soc. Am. A Opt. Image Sci.*, *18*(2), 338–351.

Emardson, T. R., M. Simons, and F. H. Webb (2003), Neutral atmospheric delay in interferometric synthetic aperture radar applications: Statistical description and mitigation, *J. Geophys. Res.*, *108*(B5), 2231, doi:10.1029/2002JB001781.

Farr, T. G., et al. (2007), The Shuttle Radar Topography Mission, *Rev. Geophys.*, *45*, RG2004, doi:10.1029/2005RG000183.

Fattahi, H. (2015), Geodetic imaging of tectonic deformation with InSAR, PhD dissertation, Univ. of Miami, Miami, Fla.

Fattahi, H., and F. Amelung (2013), DEM error correction in InSAR time series, *IEEE Trans. Geosci. Remote Sens.*, *51*(7), 4249–4259, doi:10.1109/TGRS.2012.2227761.

Fattahi, H., and F. Amelung (2014), InSAR uncertainty due to orbital errors, *Geophys. J. Int.*, *199*(1), 549–560, doi:10.1093/gji/ggu276.

Fattahi, H., and F. Amelung (2015), InSAR bias and uncertainty due to the systematic and stochastic tropospheric delay, *J. Geophys. Res. Solid Earth*, *120*, 8758–8773, doi:10.1002/2015JB012419.

Fay, N. P., and E. D. Humphreys (2005), Fault slip rates, effects of elastic heterogeneity on geodetic data, and the strength of the lower crust in the Salton Trough region, southern California, *J. Geophys. Res.*, *110*, B09401, doi:10.1029/2004JB003548.

Ferretti, A., C. Prati, and F. Rocca (2001), Permanent scatterers in SAR interferometry, *IEEE Trans. Geosci. Remote Sens.*, *39*(1), 8–20.

Fialko, Y. (2006), Interseismic strain accumulation and the earthquake potential on the southern San Andreas fault system, *Nature*, *441*(7096), 968–971, doi:10.1038/nature04797.

Field, E. H., et al. (2014), Uniform California Earthquake Rupture Forecast, Version 3 (UCERF3)—The Time-Independent Model, *Bull. Seismol. Soc. Am.*, *104*(3), 1122–1180, doi:10.1785/0120130164.
Freed, A. M., Ali, S. T., and Bürgmann, R. (2007), Evolution of stress in Southern California for the past 200 years from coseismic, postseismic and interseismic stress changes, *Geophys. J. Int.*, *169*(3), 1164–1179.
Fumal, T. E., R. J. Weldon, G. P. Biasi, T. E. Dawson, G. G. Seitz, W. T. Frost, and D. P. Schwartz (2002), Evidence for large earthquakes on the San Andreas fault at the Wrightwood, California, paleoseismic site: AD 500 to present, *Bull. Seismol. Soc. Am.*, *92*(7), 2726–2760.
Gold, P. O., W. M. Behr, D. Rood, W. D. Sharp, T. K. Rockwell, K. Kendrick, and A. Salin (2015), Holocene geologic slip rate for the Banning strand of the southern San Andreas Fault, southern California, *J. Geophys. Res. Solid Earth*, *120*, doi:10.1002/2015JB012004.
Gourmelen, N., F. Amelung, and R. Lanari (2010), Interferometric synthetic aperture radar–GPS integration: Interseismic strain accumulation across the Hunter Mountain fault in the eastern California shear zone, *J. Geophys. Res.*, *115*, B09408, doi:10.1029/2009JB007064.
Hanssen, R. F. (2001), *Radar Interferometry: Data Interpretation and Error Analysis*, Kluwer Acad., Dordrecht, Netherlands.
Hooper, A., P. Segall, and H. A. Zebker (2007), Persistent scatterer interferometric synthetic aperture radar for crustal deformation analysis, with application to Volcán Alcedo, Galápagos, *J. Geophys. Res.*, *112*, B07407, doi:10.1029/2006JB004763.
Janecke, S. U., R. J. Dorsey, and D. Forand (2010), High geologic slip rates since early Pleistocene initiation of the San Jacinto and San Felipe fault zones in the San Andreas fault system: Southern California, USA, *Geol. Soc. Am. Spec. Pap.*, *475*, 1–48, doi:10.1130/2010.2475.
Johnson, H. O., D. C. Agnew, and F. K. Wyatt (1994), Present-day crustal deformation in southern California, *J. Geophys. Res.*, *99*, 23,951–23,974, doi:10.1029/94JB01902.
Johnson, K. M., G. E. Hilley, and R. Burgmann (2007), Influence of lithosphere viscosity structure on estimates of fault slip rate in the Mojave region of the San Andreas fault system, *J. Geophys. Res.*, *112*, B07408, doi:10.1029/2006JB004842.
Jolivet, R., R. Grandin, C. Lasserre, M.-P. Doin, and G. Peltzer (2011), Systematic InSAR tropospheric phase delay corrections from global meteorological reanalysis data, *Geophys. Res. Lett.*, *38*, L17311, doi:10.1029/2011GL048757.
Kendrick, K. J., D. M. Morton, S. G. Wells, and R. W. Simpson (2002), Spatial and temporal deformation along the northern San Jacinto fault, southern California: Implications for slip rates, *Bull. Seismol. Soc. Am.*, *92*, 2782–2802, doi:10.1785/0120000615.
Li, Z., E. J. Fielding, P. Cross, and J. P. Muller (2006), Interferometric synthetic aperture radar atmospheric correction: GPS topography-dependent turbulence model, *J. Geophys. Res.*, *111*, B02404, doi:10.1029/2005JB003711.
Li, Z., E. J. Fielding, P. Cross, and R. Preusker (2009), Advanced InSAR atmospheric correction: MERIS/MODIS combination and stacked water vapour models, *Int. J. Remote Sens.*, *30*(13), 3343–3363.
Li, Z. W., Xu, W. B., Feng, G. C., Hu, J., Wang, C. C., Ding, X., and Zhu, J. J. (2012), Correcting atmospheric effects on InSAR with MERIS water vapour data and elevation-dependent interpolation model, *Geophys. J. Int.*, *189*(2), 898–910, doi:10.1111/j.1365-246X.2012.05432.x.
Lin, Y. N., M. Simons, E. A. Hetland, P. Muse, and C. DiCaprio (2010), A multiscale approach to estimating topographically correlated propagation delays in radar interferograms, *Geochem. Geophys. Geosyst.*, *11*, Q09002, doi:10.1029/2010GC003228.
Lindsey, E. O., and Y. Fialko (2013), Geodetic slip rates in the southern San Andreas Fault system: Effects of elastic heterogeneity and fault geometry, *J. Geophys. Res. Solid Earth*, *118*, 689–697, doi:10.1029/2012JB009358.
Liu, S., Z.-K. Shen, and R. Bürgmann (2015), Recovery of secular deformation field of Mojave Shear Zone in Southern California from historical terrestrial and GPS measurements, *J. Geophys. Res. Solid Earth*, *120*, 3965–3990, doi:10.1002/2015JB011941.
Liu, Z., H.-S. Jung, and Z. Lu (2014), Joint correction of ionosphere noise and orbital error in L-band SAR interferometry of interseismic deformation in Southern California, *IEEE Trans. Geosci. Remote Sens.*, *52*(6), 3421–3427, doi:10.1109/TGRS.2013.2272791.
Lohman, R. B., and M. Simons (2005), Some thoughts on the use of InSAR data to constrain models of surface deformation: Noise structure and data downsampling, *Geochem. Geophys. Geosyst.*, *6*, Q01007, doi:10.1029/2004GC000841.
Lundgren, P., E. A. Hetland, Z. Liu, and E. J. Fielding (2009), Southern San Andreas-San Jacinto fault system slip rates estimated from earthquake cycle models constrained by GPS and interferometric synthetic aperture radar observations, *J. Geophys. Res.*, *114*, B02403, doi:10.1029/2008JB005996.
Marinkovic, P., and Y. Larsen (2013), Consequences of long-term ASAR local oscillator frequency decay—An empirical study of 10 years of data, *Proceedings of the Living Planet Symposium*, European Space Agency, Edinburgh, U. K.
Matsu'ura, M., D. D. Jackson, and A. Cheng (1986), Dislocation model for aseismic crustal deformation at Hollister, California, *J. Geophys. Res.*, *91*, 2661–2674.
McCaffrey, R. (2002), Crustal block rotations and plate coupling, in *Plate Boundary Zones*, edited by S. Stein and J. Freymueller, pp. 101–122, AGU, Washington, D. C.
McCalpin, J. P. (Ed.) (2009), *Paleoseismology, Int. Geophys. Ser.*, vol. 95, Academic, San Diego, Calif.
Meade, B. J., and B. H. Hager (2005), Block models of crustal motion in southern California constrained by GPS measurements, *J. Geophys. Res.*, *110*, B03403, doi:10.1029/2004JB003209.
Meyer, F., and J. Nicoll (2008), The Impact of the Ionosphere on Interferometric SAR Processing, *IEEE International Geoscience and Remote Sensing Symposium*, pp. II-391–II-394, IEEE, Boston, Mass.
Murray, J., R. Lohman, and D. Sandwell (2013), Combining GPS and Remotely Sensed Data to Characterize Time-Varying Crustal Motion, *Eos Trans. AGU*, *94*(35), 309–309.
Murray, J. R., S. E. Minson, and J. L. Svarc (2014), Slip rates and spatially variable creep on faults of the northern San Andreas system inferred through Bayesian inversion of Global Positioning System data, *J. Geophys. Res. Solid Earth*, *119*, 6023–6047, doi:10.1002/2014JB010966.
Onn, F., and H. A. Zebker (2006), Correction for interferometric synthetic aperture radar atmospheric phase artifacts using time series of zenith wet delay observations from a GPS network, *J. Geophys. Res.*, *111*, B09102, doi:10.1029/2005JB004012.
Otten, M., C. Flohrer, T. Springer, and W. Enderle (2012), Generating precise and homogeneous orbits for ERS-1, ERS-2, Envisat, Cryosat-2, Jason-1 and Jason-2, in *Proceedings of the 20 Years Progress in Radar Altimetry Symposium*, Venice, Italy.
Pepe, A., and R. Lanari (2006), On the extension of the minimum cost flow algorithm for phase unwrapping of multitemporal differential SAR interferograms, *IEEE Trans. Geosci. Remote Sens.*, *44*(9), 2374–2383, doi:10.1109/TGRS.2006.873207.
Platt, J. P., and T. W. Becker (2010), Where is the real transform boundary in California?, *Geochem. Geophys. Geosyst.*, *11*, Q06012, doi:10.1029/2010GC003060.
Pollitz, F. F. (2015), Postearthquake relaxation evidence for laterally variable viscoelastic structure and water content in the Southern California mantle, *J. Geophys. Res. Solid Earth*, *120*, 2672–2696, doi:10.1002/2014JB011603.
Puysségur, B., R. Michel, and J.-P. Avouac (2007), Tropospheric phase delay in interferometric synthetic aperture radar estimated from meteorological model and multispectral imagery, *J. Geophys. Res.*, *112*, B05419, doi:10.1029/2006JB004352.
Remy, D., S. Bonvalot, P. Briole, and M. Murakami (2003), Accurate measurements of tropospheric effects in volcanic areas from SAR interferometry data: Application to Sakurajima volcano (Japan), *Earth Planet. Sci. Lett.*, *213*(3), 299–310.

Rockwell, T., C. Loughman, and P. Merifield (1990), Late Quaternary rate of slip along the San Jacinto Fault Zone near Anza, southern California, *J. Geophys. Res.*, *95*, 8593–8605, doi:10.1029/JB095iB06p08593.

Rosen, P. A., S. Hensley, H. A. Zebker, F. H. Webb, and E. J. Fielding (1996), Surface deformation and coherence measurements of Kilauea Volcano, Hawaii, from SIR-C radar interferometry, *J. Geophys. Res.*, *101*, 23,109–23,125.

Rosen, P. A., S. Hensley, G. Peltzer, and M. Simons (2004), Update repeat orbit interferometry package released, *Eos Trans. AGU*, *85*, 47.

Rudenko, S., M. Otten, P. Visser, R. Scharroo, T. Schöne, and S. Esselborn (2012), New improved orbit solutions for the ERS-1 and ERS-2 satellites, *Adv. Space Res.*, *49*(8), 1229–1244.

Savage, J. C., and R. O. Burford (1973), Geodetic determination of relative plate motion in Central California, *J. Geophys. Res.*, *78*, 832–845.

Savage, J. C., and W. H. Prescott (1978), Asthenosphere readjustment and the earthquake cycle, *J. Geophys. Res.*, *83*, 3369–3376, doi:10.1029/JB083iB07p03369.

Segall, P. (2002), Integrating geologic and geodetic estimates of slip rate on the San Andreas fault system, *Int. Geol. Rev.*, *44*(1), 62–82.

Shen, Z. K., R. W. King, D. C. Agnew, M. Wang, T. A. Herring, D. Dong, and P. Fang (2011), A unified analysis of crustal motion in southern California, 1970–2004: The SCEC crustal motion map, *J. Geophys. Res.*, *116*, B11402, doi:10.1029/2011JB008549.

Shirzaei, M., and R. Burgmann (2012), Topography correlated atmospheric delay correction in radar interferometry using wavelet transforms, *Geophys. Res. Lett.*, *39*, L01305, doi:10.1029/2011GL049971.

Shirzaei, M., and R. Bürgmann (2013), Time-dependent model of creep on the Hayward fault from joint inversion of 18 years of InSAR and surface creep data, *J. Geophys. Res. Solid Earth*, *118*, 1733–1746, doi:10.1002/jgrb.50149.

Spinler, J. C., R. A. Bennett, M. L. Anderson, S. F. McGill, S. Hreinsdóttir, and A. McCallister (2010), Present-day strain accumulation and slip rates associated with southern San Andreas and eastern California shear zone faults, *J. Geophys. Res.*, *115*, B11407, doi:10.1029/2010JB007424.

Tarayre, H., and D. Massonnet (1996), Atmospheric propagation heterogeneities revealed by ERS-1 interferometry, *Geophys. Res. Lett.*, *23*, 989–992.

Tizzani, P., P. Berardino, F. Casu, P. Euillades, M. Manzo, G. P. Ricciardi, G. Zeni, and R. Lanari (2007), Surface deformation of Long Valley Caldera and Mono Basin, California, investigated with the SBAS-InSAR approach, *Remote Sens. Environ.*, *108*(3), 277–289, doi:10.1016/j.rse.2006.11.015.

Tong, X., D. T. Sandwell, and B. R. Smith-Konter (2013), High-resolution interseismic velocity data along the San Andreas Fault from GPS and InSAR, *J. Geophys. Res. Solid Earth*, *118*, 369–389, doi:10.1029/2012JB009442.

Van der Woerd, J., Y. Klinger, K. Sieh, P. Tapponnier, F. J. Ryerson, and A.-S. Mériaux (2006), Long-term slip rate of the southern San Andreas Fault from 10Be- 26Al surface exposure dating of an offset alluvial fan, *J. Geophys. Res.*, *111*, B04407, doi:10.1029/2004JB003559.

Wadge, G., et al. (2002), Atmospheric models, GPS and InSAR measurements of the tropospheric water vapour field over Mount Etna, *Geophys. Res. Lett.*, *29*(19), 1905, doi:10.1029/2002GL015159.

Walters, R. J., J. R. Elliott, Z. Li, and B. E. Parsons (2013), Rapid strain accumulation on the Ashkabad fault (Turkmenistan) from atmosphere-corrected InSAR, *J. Geophys. Res. Solid Earth*, *118*, 3674–3690, doi:10.1002/jgrb.50236.

Wang, T., and S. Jonsson (2014), Phase-Ramp reduction in interseismic interferograms from pixel-offsets, *IEEE J. Selec. Top. Appl. Earth Observ. Remote Sens.*, *7*(5), 1709–1718.

Webley, P. W., R. M. Bingley, A. H. Dodson, G. Wadge, S. J. Waugh, and I. N. James (2002), Atmospheric water vapour correction to InSAR surface motion measurements on mountains: Results from a dense GPS network on Mount Etna, *Phys. Chem. Earth, Parts A/B/C*, *27*(4), 363–370.

Williams, S., Y. Bock, and P. Fang (1998), Integrated satellite interferometry: Tropospheric noise, GPS estimates and implications for interferometric synthetic aperture radar products, *J. Geophys. Res.*, *103*, 27,051–27,067.

Wright, T. J., B. E. Parsons, and Z. Lu (2004), Toward mapping surface deformation in three dimensions using InSAR, *Geophys. Res. Lett.*, *31*, L01607, doi:10.1029/2003GL018827.

Wright, T. J., J. R. Elliott, H. Wang, and I. Ryder (2013), Earthquake cycle deformation and the Moho: Implications for the rheology of continental lithosphere, *Tectonophysics*, *609*, 504–523, doi:10.1016/j.tecto.2013.07.029.

Zebker, H. A., P. A. Rosen, and S. Hensley (1997), Atmospheric effects in interferometric synthetic aperture radar surface deformation and topographic maps, *J. Geophys. Res.*, *102*, 7547–7563.

Zeng, Y., and Z.-K. Shen (2014), Fault network modeling of crustal deformation in California constrained using GPS and geologic observations, *Tectonophysics*, *612-613*, 1–14.

Journal of Geophysical Research

Supporting Information for

Potential and limits of InSAR to characterize interseismic deformation independently of GPS data: application to the southern San Andreas Fault system

E. Chaussard [(1)], C.W. Johnson [(2,3)], R. Bürgmann [(2,3)], and H. Fattahi [(4)]

)

(1) Department of Geology, State University of New York, Buffalo, New York

(2) Department of Earth and Planetary Science, University of California, Berkeley, Berkeley, California

(3) Berkeley Seismological Laboratory, University of California, Berkeley, California

(4) Seismological Laboratory, California Institute of Technology, Pasadena, California

Contents of this file

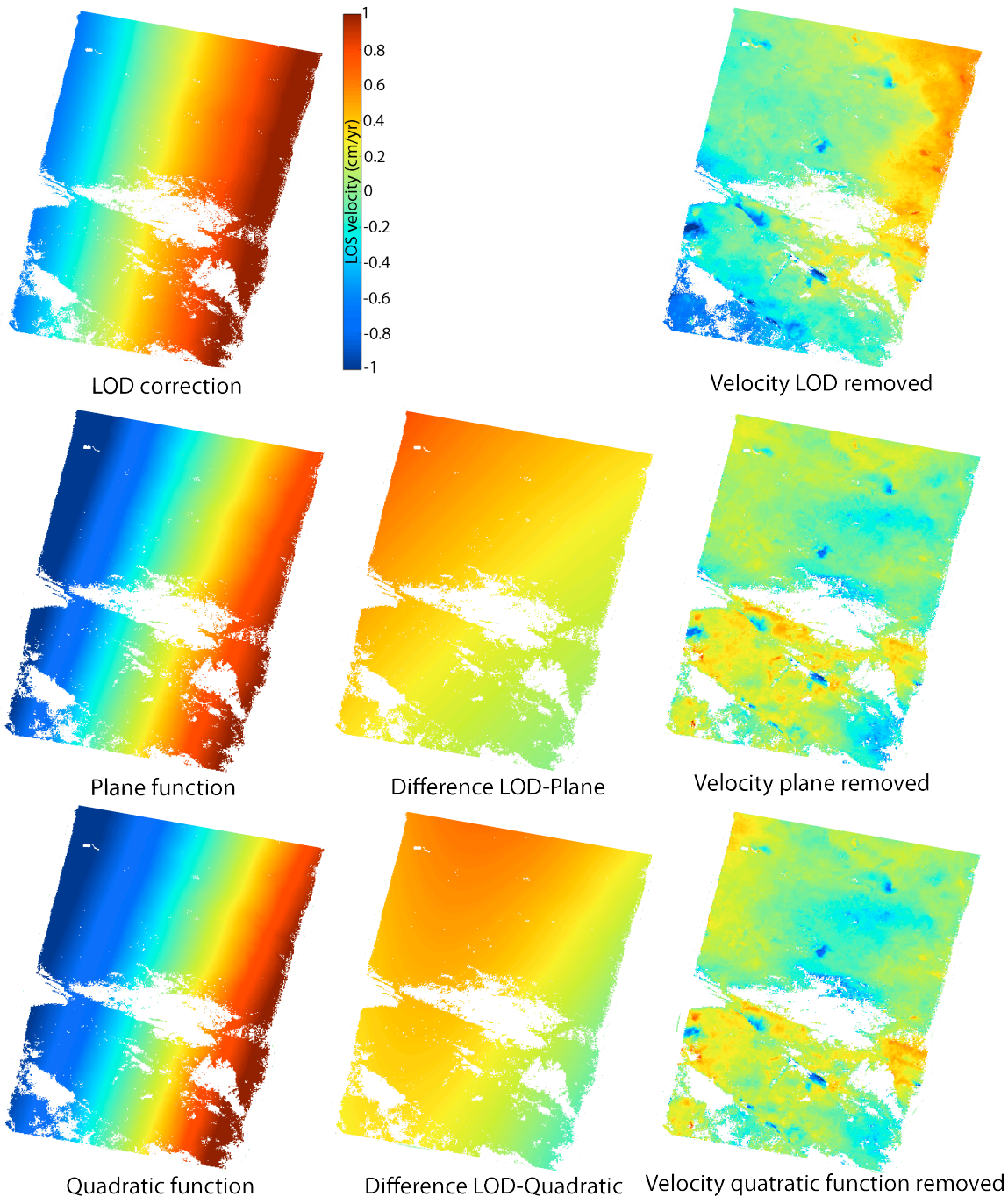

Figure S1. Comparison between the LOD correction using the empirical model of Marinkovic and Larsen [*2013*] and the effect of removing a plane or a quadratic function to each interferogram. The mean velocity map resulting from the LOD correction contains long-wavelength deformation while the ones resulting from removal of planes and quadratic function do not.

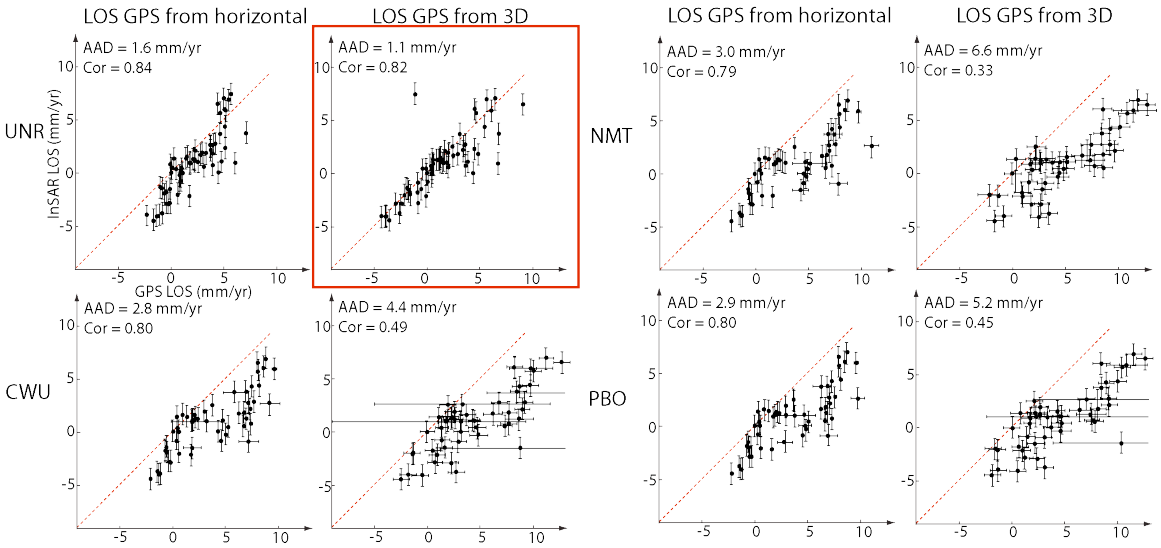

Figure S2. Same as Figure 7 but using GPS velocities produced by the processing centers rather than recalculated from the GPS time series for the same time period as the InSAR data. The agreement between the InSAR and GPS data is significantly decreased as shown by the lower correlation values (due to off-plot velocities) and the increased average absolute deviation (AAD). This increased misfit is likely due to additional corrections applied to the GPS velocities such as atmospheric and postseismic corrections.

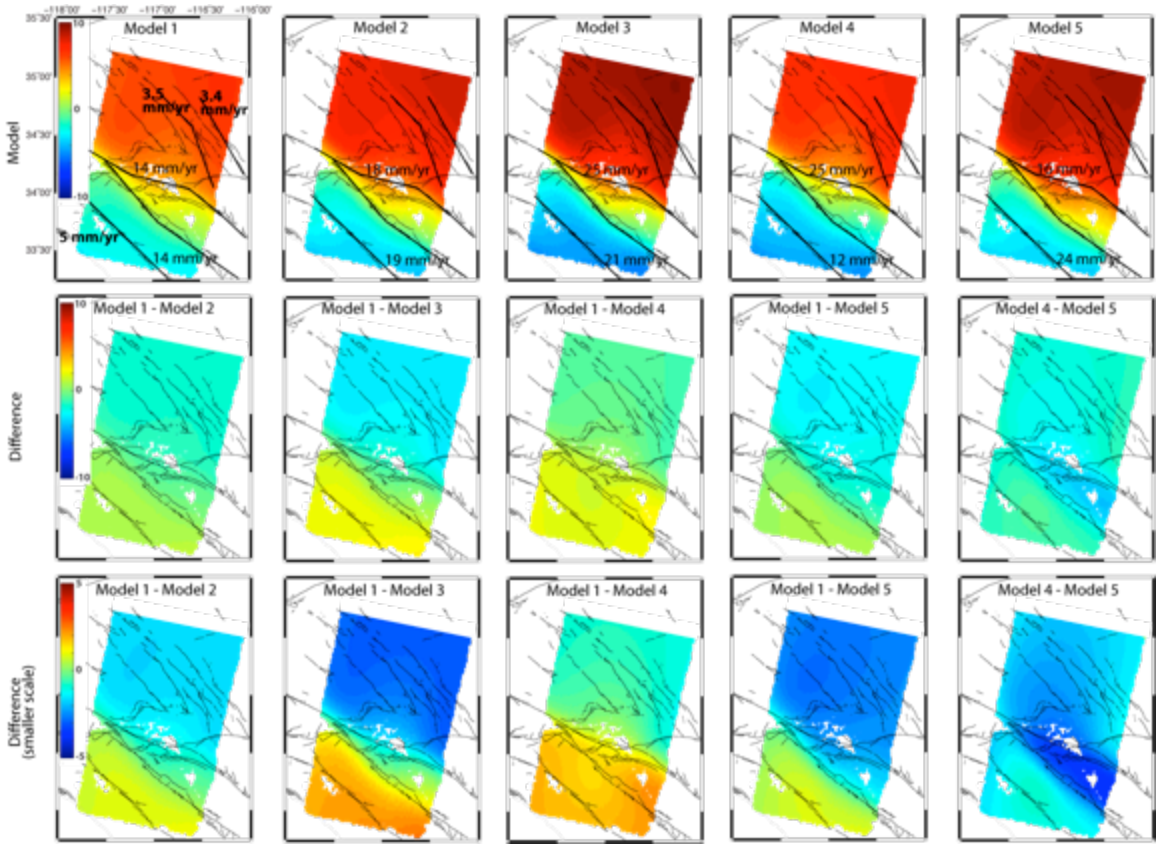

Figure S3. Top row: mean LOS velocity maps produced by forward dislocation models considering five different slip scenarios for the SAF and SJF: from left to right, 14 mm/yr of slip on SAF and SJF (model 1), 18 mm/yr on SAF and 19 mm/yr on SJF (model 2), 25 mm/yr on SAF and 21 mm/yr on SJF (model 3), 25 mm/yr on SAF and 12 mm/yr on SJF (model 4), and 16 mm/yr on SAF and 24 mm/yr on SJF (model 5). Middle row: difference between the different mean velocity maps with the same color scale. Bottom row: same as middle row with a color scale of ±5 mm/yr.

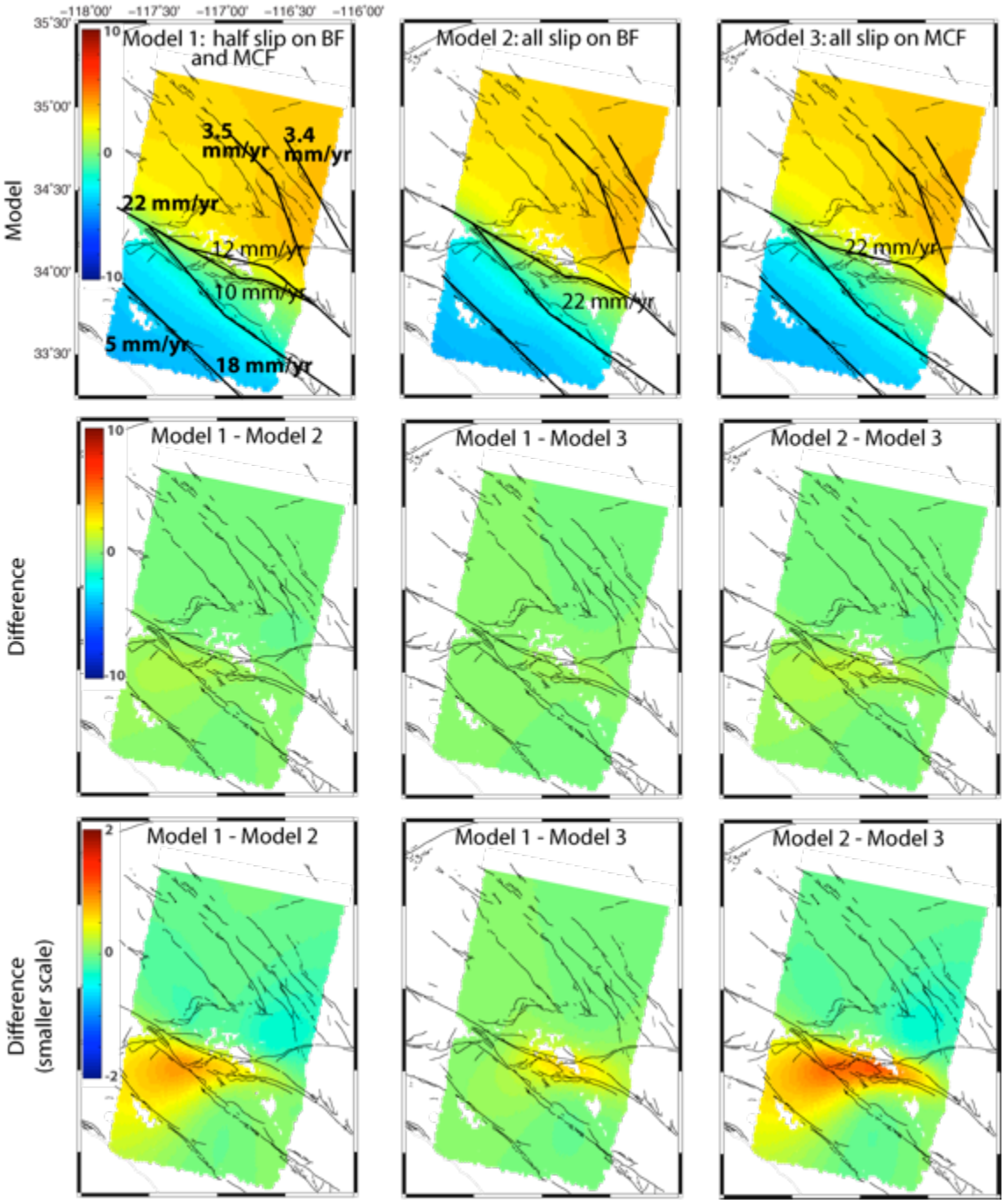

Figure S4. Top row: mean LOS velocity maps produced by forward dislocation models considering different slip scenarios for the BF and MCF: 10 mm/yr on BF and 12 mm/yr on MCF (left), 22 mm/yr on BF and 0 mm/yr on MCF (center), and 0 mm/yr on BF and 22 mm/yr on MCF (right). Middle row: difference between the mean velocity maps with the same color scale. Bottom row: same as middle row with a color scale of ±2 mm/yr.

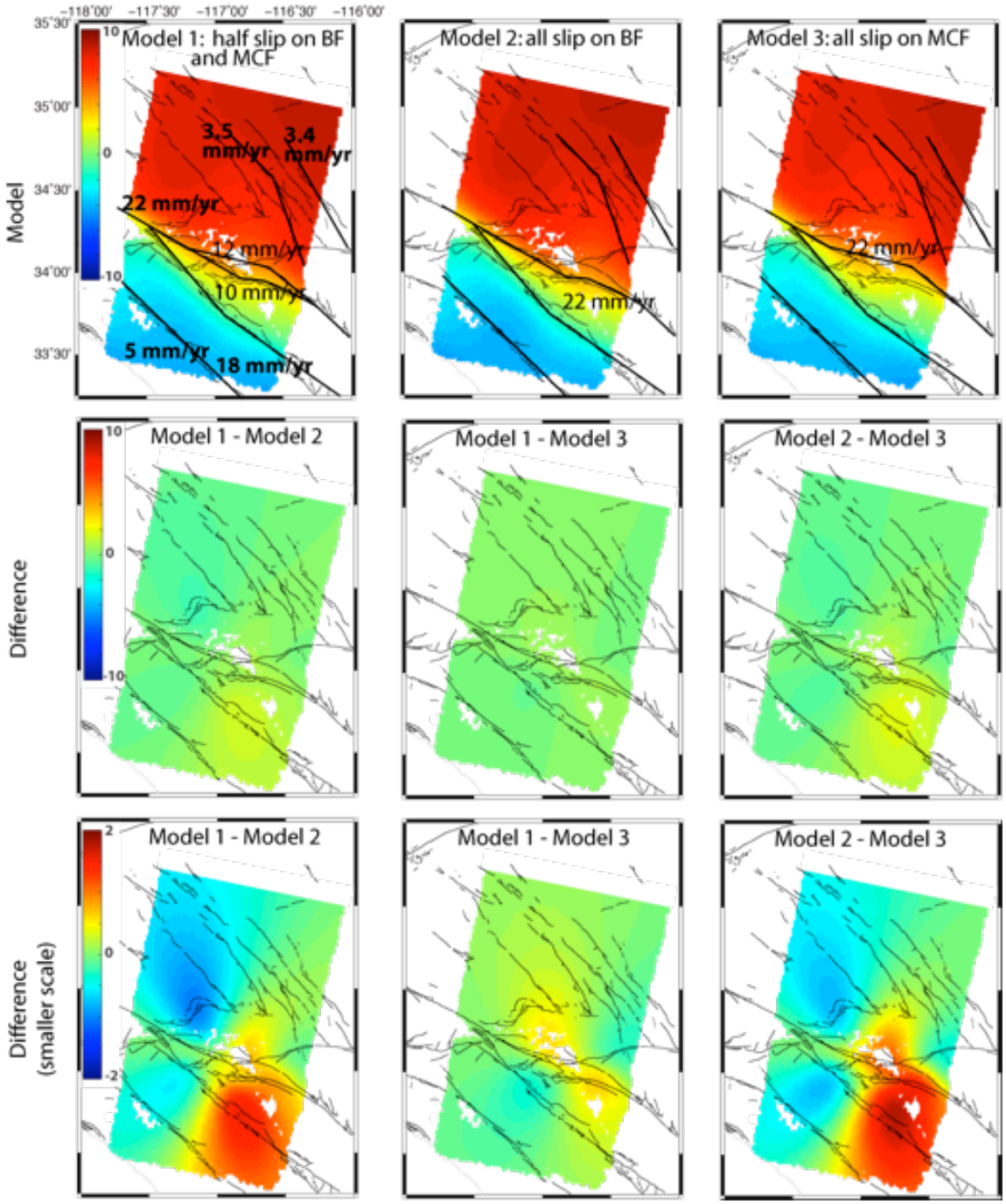

Figure S5. Same as Figure S4 but for mean velocity maps projected into fault parallel motion for BF and MCF.

050530-051226	070219-070709	071126-080901	080901-081110
050530-060306	070219-070813	071126-081110	081110-090608
050530-060515	070219-071126	071231-080310	081110-090713
050912-051121	070219-080204	080204-080310	081110-090817
050912-051226	070219-080310	080204-080414	081110-091026
050912-060306	070709-070813	080204-080519	081110-091130
050912-060515	070709-071126	080204-080623	090608-090713
051121-051226	070709-071231	080204-080728	090608-090921
051121-060619	070709-080310	080204-081110	090608-100208
051121-061211	070709-080519	080310-080519	090713-090817
051226-060306	070813-071126	080310-080623	090713-091026
051226-060515	070813-071231	080310-081110	090713-091130
051226-060619	070813-080204	080414-080519	090713-100524
060306-060515	070813-080310	080414-080623	090817-091026
060306-060619	070813-080519	080414-080728	090817-091130
060306-070219	070813-080623	080414-081110	090817-100315
060515-060619	070917-071126	080519-080623	090817-100524
060515-061211	070917-080204	080519-080728	090921-100208
060515-070219	070917-080414	080519-081110	091026-091130
060619-061211	070917-080623	080623-080728	091026-100315
060619-070115	070917-080728	080623-081110	091026-100524
060619-070219	071126-080204	080623-090608	091130-100315
061211-070115	071126-080310	080623-090713	091130-100524
061211-070219	071126-080414	080728-081110	100315-100524
061211-070917	071126-080519	080728-090608	
061211-071126	071126-080623	080728-090713	
070115-070917	071126-080728	080728-090817	

Table S1. List of the interferograms used in the coherence-based selection time series analysis. The dates are written in the format YYMMDD.